Electronic ISSN: 1309-0267

International Journal of Engineering & Applied Sciences

IJEAS

Volume 12, Issue 1
2020

Published by Akdeniz University

Editorial Board

(The name listed below is not Alphabetical or any title scale)

Abstracting & Indexing

IJEAS provides unique **DOI** link to every paper published.

Editorial Scope

The journal presents its readers with broad coverage across some branches of engineering and science of the latest development and application of new solution algorithms, artificial intelligent techniques innovative numerical methods and/or solution techniques directed at the utilization of computational methods in solid and nano-scaled mechanics.

International Journal of Engineering & Applied Sciences (IJEAS) is an Open Access Journal

International Journal of Engineering & Applied Sciences (IJEAS) publish original contributions on the following topics:

Numerical Methods in Solid Mechanics

Nanomechanic and applications

Microelectromechanical systems (MEMS)

Vibration Problems in Engineering

Higher order elasticity (Strain gradient, couple stress, surface elasticity, nonlocal elasticity) Applied Mathematics

IJEAS allows readers to read, download, copy, distribute, print, search, or link to the full texts of articles.

CONTENTS

International Journal of Engineering & Applied Sciences (IJEAS)
Vol. 12, Issue 1 (2020) 1-14
http://dx.doi.org/10.24107/ijeas.694523
Int J Eng Appl Sci 12(1) (2020) 1-14

Matching Image Sequences using Mathematical Programming: Visual Localization Applications

Abdul Hafiz ABDULHAFIZ

Department of Computer Engineering, Hasan Kalyoncu University, Gaziantep, Turkiye
E-mail address: abdul.hafez@hku.edu.com

ORCID numbers of authors:
0000-0002-1908-5521

Received date: 25.02.2020
Accepted date: 23.04.2020

Abstract

Visual localization of a robot is to determine the location using visual input from a camera. We present in this article a new visual localization algorithm to find the robot location with respect a visual route map stored as a video sequence. The sequence of the current and past images is matched to the map, i.e. the reference image sequence, to produce the best match of the current image. The image sequence matching is achieved by measuring the similarity between the two image sequences using the dynamic time warping (DTW) algorithm. The DTW algorithm employs Dynamic Programming (DP) to calculate the distance (the cost function) between the two image sequences. Consequently, the output of the alignment process is an optimal match of each image in the current image sequence to an image in the reference one. Our proposed DTW matching algorithm is suitable to be used with a wide variety of engineered features, they are SIFT, HOG, LDP in particular. The proposed DTW algorithm is compared to other recognition algorithms like Support Vector Machine (SVM) and Binary-appearance Loop-closure (ABLE) algorithm. The datasets used in the experiments are challenging and benchmarks, they are commonly used in the literature of the visual localization. These datasets are the" Garden point", "St. Lucia", and "Nordland". The experimental observations have proven that the proposed technique can significantly improve the performance of all the used descriptors like HOG, LDB, and SIFT. The performance of these features is compared to the case of using the proposed DTW instead of the classical nearest neighbor. In addition, it was able to the SVM and ABLE localization algorithm.

Keywords: Visual localization, Image sequence matching, Dynamic programming.

1. Introduction

The visual localization techniques belong to the content-based image retrieval algorithms. It can be used for visual localization, also called Place recognition, by using the available reference sequence (experience(s) of the robot) to determine the appropriate response for the current observation. In addition, the significant improvements in the visual localization topic, leads to increase the attention of the robotics community [1-4]. Fig. 1 depicts the main components of the visual localization process. The main two components are the feature extraction and the localization algorithms. We propose in this work a localization algorithm that is based on DP, and test it with different feature extraction methods.

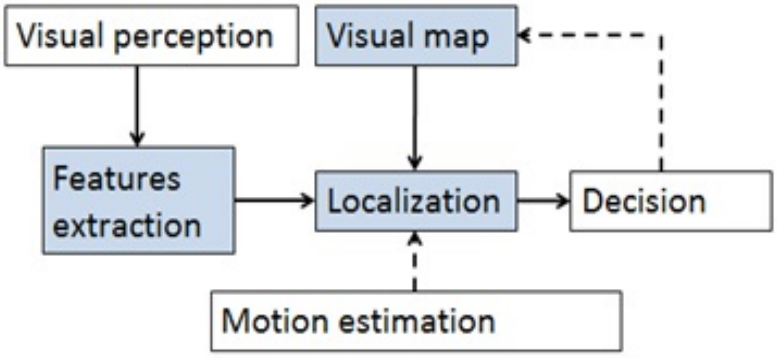

Fig. 1. Schematic diagram of the visual localization (place recognition) process showing the different components and links between them.

There are several works in the literature on visual localization and place recognition. They mainly focus on matching two or more image sequences for the purpose of localizing the object in the environment. The work called FabMap that is presented in [5], SeqSLAM presented [1], the Flow networks based algorithm presented in [6], and ABLE [7], [8] are example of the pioneering works in the topic of visual localization.

Several attempts on localization with respect to visual map that is represented using sequences of images are reported in the literature. These attempts include visual localization in crowded environment [9], [10], experience based navigation for long-term localization [11], [12], and summarizing the map of experiences for long-term localization [13]. Other methods like RTAB-Map [14], [15] focus on memory management to satisfy the real time conditions.

The contribution of this paper is mainly a novel visual localization algorithm that uses image sequence alignment for localizing mobile robots. In this work, the sequence matching and alignment is done using the Dynamic Time Warping (DTW). In addition, a set of common handcrafted features used to compare the proposed algorithm with two of the-state-of-the-art algorithms. These are the ABLE and SVM ones. The validation process for the developed approach and the experimental study were performed using some common benchmark datasets.

2. Review of Previous Works

The RTAB-Map presented in [14], [15] works fine with the loop closure problem solving issues like when the map is large enough to slow the system down. RTAB-Map track SURF features using discrete Kalman filter without dealing with processes of matching and retrieving multiple images which are the core of our proposals. Our main focus, in contrast, is on localization in environments that show considerable changes in its representation.

FabMap localization algorithm system [16] is topological pure image retrieval that use probabilistic model to update the vocabulary of the image retrieval. Image retrieval techniques are borrowed from computer vision community [17] in which a set of selected features are stored in a dictionary of vocabularies, while the reference images are sorted using inverted index techniques. In particular, the inverted index is updated to accommodate new positively observed features. FabMap is a data driven approach to calculate the observation likelihood. It uses a bag-of-word of SIFT features model to describe the distinctiveness of each feature during the learning stage. There still is a scalability problem with bag-of-words model since it needs large number of vocabularies for larger environments.

Visual localization in crowded environment from multiple experiences was proposed in [9], [10]. The work addresses the case where the vehicle frequently visits the same environment updating it's a priori knowledge after each visit. A bag-of-words model along with a weighted inverted index are employed as a map of the considered environment. The aim was to learn useful visual features and visually stable features that are static in the environment by assigning a weight to each feature. In this work, the visual map is suggested to store several reference image sequences since cyclic appearance changes require more than one representation model.

Long-term localization is achieved based on visual experience as presented in [12]. The visual experiences here are stored as a series of visual odometry data attached to a sequence of visual images. A new experience is created and stored after each visit to non-recognized place. This is noted as failure of all localizer which are associated with the multiple experiences stored in the map. The experiences are connected to each other via GPS priors or geometric consistency among image frames. However, they do not systematically explore the connectivity between experiences. Hence, a few nodes are connected in each experience depends on whether an accurate GPS data is available or not for example.

Multiple experiences case is also considered in [11]. Here, a probabilistic cost map is created in a self-supervised manner using a Gaussian process. Multiple representations of the environment in the visual map are used here to describe the travers-ability of the environment rather than to localize the robot. The Gaussian process model is successfully used to plan a path for the robot through traversable areas. A summary map is proposed in [18] as a solution for the mapping from multiple sequences problem, in which scoring functions are used, similarly to [9], [10], to update the summary map after every arrival of new experience. The scoring function is used to evaluate the usefulness of the landmarks and trajectory segments. Those have high score are retained in the summary map while others are forgotten. However, these methods represent fine-grained information about the environment, but do not consider any appearance aspects since it does not store whole image information, that what is done in our proposal.

FabMap considers the localization problem as a visual loop closure problem. On the other hand, the SeqSLAM algorithm [1] using and searching all possible visual maps matching to solve the localization problem. Overall, the variations of view and camera poses can badly affect the performance of such a technique. A recent impressive visual localization using sequence matching and consider the problem as an alignment of two sequences of images were presented in [6]. This approach works on minimizing the cost of the high computational complexity flow network. In more details, it uses the ABLE algorithm [7], to represent the sequences of images as binary code, then, the effect of changes in appearance while taking the images was reduced using the Illumination invariance color.

Recently, SVM was able to archive a good performance as a classifier in many filed such as object classification, image matching, etc. In [19], some vision-based techniques for visual place recognition were introduced. First, an image salience generation was adapted to improve the single image-based matching. Then, the Support Vector Machines (SVMs) was used to filter the outliers from both the reference and test datasets. In [20] the Kernel Principal Component Analysis (KPCA) was used to extract the image features. In more details, the SIFT features from a given image is extracted, then, the minimum Euclidean is used to find the distance between the extracted features and the visual codebook that was constructed offline by K-means. In the approach of [20], SVM was used for data analysis as a classifier. In [21], both HOG and LBP were used for visual localization.

3. Dynamic Programming and Dynamic Time Warping

DP aims at solving the problem in hand by combining the individual solutions to smaller problems that are sub problems of the original problem [22]. DP efficiently solves such subproblems when these subproblems overlap. In other words, when these subproblems are sharing another lower level subproblems like subsubproblems, and so on. A DP algorithm provide a solution to each of these subsubproblem, which is stored in a table matrix to avoid solving the same individual problem again.

The DTW algorithm has applications in several areas. Its applications are increasing since it was first introduced and developed in the 60s and 70s of the last century till today. Its application was initially explored to solve the speech recognition problem [23], [24], but it currently has applications in topics like: online and offline handwriting and signature verification [25], [26], sign language recognition [27], mining and searching databases of time series [28], [29], image understanding and computer graphics [30], surveillance [31], matching protein sequences in bioinformatics [32], and music applications [33].

DTW algorithm has become much popular his efficient solutions to the time series problems. It measures the similarity between two sequences by minimizing a cost function in order to detect their shape similarity over different times, i.e. they have different phases.

Let us have two time sequences $X = (x_1, x_2, \dots, x_n)$, where $n \in N$ and $Y = (y_1, y_2, \dots, y_m)$, where $m \in N$. Here, N is the group of natural numbers. DTW produces an optimal solution with a time complexity in the order of $O(MN)$. The data sequences must be sampled evenly at a uniform basis, so sometimes a resampling stage in the feature space is needed.

To compare these two different sequences X and Y using DTW, we need to use a local distance measure between two values x_i, y_j each from one sequence. This distance can be defined as a function $D(x_i, y_j) \in R$, where R is the real numbers. The value of the distance function between two elements from the sequences X and Y is smaller when they are more similar, and is larger when they are more different. Since DTW is a Dynamic Programming based algorithm, it is more convenient to call this distance function as the "cost function". Consequently, the process of finding the optimal alignment between the two sequences is becoming the arranging of the two sequences by optimizing the cost function.

3.1. Sequence Alignment using DTW

In this subsection, the mechanism of aligning the main two image sequences is explained. One of the sequences is $Y = \{y_j\}$ that is the reference one, here $j = (1, \dots, m)$, and the second sequence is the test that denoted by $X = \{x_i\}$ where $i = (1, \dots, n)$, this process uses the DTW, and as a first step, we build the cost matrix C. In general, as shown in Equation (2), the elements of the distance matrix are accumulated to obtain the cost matrix. Note that n represent the lengths of test sequence and m the lengths of the reference sequence.

In DTW, matrix C refers to the cumulative distance, i.e., $D(\mathrm{i}, \mathrm{j}) + Mcd$, where $D(\mathrm{i}, \mathrm{j})$ is the distance between currently matching two images. The $Mcd(\mathrm{i}, \mathrm{j})$ is the smaller distance $D(\mathrm{i}, \mathrm{j})$ among the images in surrounding neighborhood. It can formulated as in Equation (1):

$$Mcd(\mathrm{i},\mathrm{j}) = \min\begin{Bmatrix} D(\mathrm{i}-1,\mathrm{j}) \\ D(\mathrm{i},\mathrm{j}-1) \\ D(\mathrm{i}-1,\mathrm{j}-1) \end{Bmatrix}, \quad (1)$$

Then, the cost matrix C is filled by dynamic programming by implying the following relation:

$$C\ (\mathrm{i},\mathrm{j}) = D(\mathrm{i},\mathrm{j}) + Mcd(\mathrm{i},\mathrm{j}) \quad (2)$$

After filling the matrix C, the optimal path $P = \{p_k\}$, where $k = (1, \dots, L)$ is found by DTW. Hence, whenever images $x(i_k)$ and $y(j_k)$ are found to be a part of the optimal path P, they are represented by $p_k = (i_k, j_k)$.

It is worth mentioning that by back-tracing the matrix C and choosing the lowest cumulative distance of the previous elements we define what is called the optimal path. Hence, by minimizing the following function, we can obtain the optimal path, i.e., the path through the elements of the matrix C . These matrix elements have the minimum accumulated cost values $C\ (\mathrm{i},\mathrm{j})$.

$$\mathrm{Q(P)} = \sum_{l=1}^{L} C(i_l, j_l) \quad (3)$$

For more details about DTW, the reader is referred to [24], [34] and [35]. Fortunately, even after integrating the DTW, the complexity of our approach is reasonable as compared with other existing approaches and as compared with the improvement that has been archived by integrating the DTW. In other words, complexity equals $O(m{\times}u)$, whereas mentioned before m is the lengths of the reference sequence and u is the number of images in the optimal path. As a result, since u is much less than n, DTW decreases the number of required comparisons. However, the complexity of Flow network algorithm, the well common another matching algorithm, is estimated as $O(n{\times}m)$. In more details, the redaction in the complexity came from the sequential nature that applied by DTW, i.e., when a test image arrives let say $x(i)$, it will be compared with the sequence of reference images which has the same or lager index $(j, \text{where j} >= \text{i})$. It is worth mentioning that in this work the vehicle can move forward only, and allowing the vehicle to other directions can be done as future work. The diagram of the proposed sequence method is shown in Fig. 2.

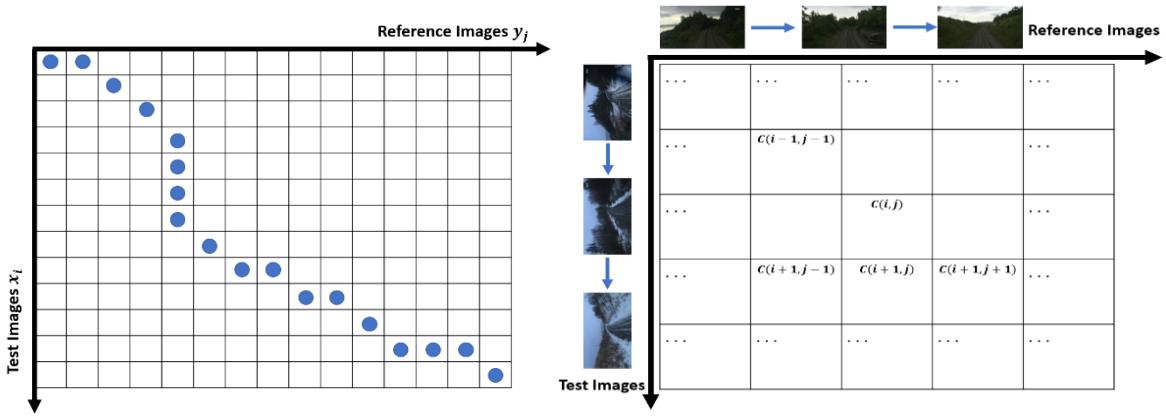

(a) (b)

Fig. 2. This figure shows calculating the cost matrix element C (i, j) for matching mage xi with reference image y_j in (a), while the corresponding optimal matching path is shown in (b).

4. Sequence Matching Method for Visual Localization

In general, image matching/alignment has been used frequently for visual place recognition, however, its efficiency and execution time can be effected by the size of the used visual dataset and it is impractical for processing large visual datasets. In this paper, we have solved this problem by integrating the DTW into the image matching/alignment [24].

4.1. Image Features Presentation and their Distances

Three of the most popular handcrafted descriptors are used. These are the local difference binary features (LDB), the scale-invariant feature transform (SIFT), and the histogram of gradient (HOG), however, any other descriptor(s) can be integrated into the proposed algorithm. The used descriptors is summarized in the following:

SIFT: This descriptor work on detecting the image's key points which can be considered as the most important regions. Then, the appearance of these key points is characterized by a 3-D spatial histogram.

HOG: This descriptor starts by dividing the image into small squared cells, where each cell is then represented by a histogram of oriented gradients. Then the block-wise pattern is used to normalize the results obtained from the previous step.

LDB: This descriptor represents each image by a binary string. It firstly extracts the patches from the image. After that, the differences in the gradient and intensityare tested used to find the binary string. This process is done for a pairs of grid cells for each patch.

Based on the above, the distance between the feature vectors are given as

$$D(\mathrm{i},\mathrm{j}) \;=\; Distance(\mathrm{xi},\mathrm{yj}) = 1 - \frac{|Ax_i| \;.\; |Ay_i|}{\|Ax_i\| \;.\; \|Ay_j\|} \tag{4}$$

Here, the vectors Ax_i and Ay_i are extracted from images x_i and y_j. Also, the element $D(\mathrm{i},\mathrm{j})$ represents the distance between matching the test image x_i and the reference image y_j.

It is worth mentioning that related to the LDB descriptor, as it produces a binary vector, it has been proven that it is preferred to use Hamming distance with LDB. Hence, we have used the Hamming distance to represent the distance matrix $D(\mathrm{i},\mathrm{j})$ whenever LDB is used in this study, Hamming distance is given as

$$D(\mathrm{i},\mathrm{j}) \;=\; Distance(x_i, y_j) = Ax_i \oplus Ay_i \tag{5}$$

Finally, independent of the selected cost function, as soon as the elements of $D(\mathrm{i},\mathrm{j})$ are calculated, the same steps will be allows used by DTW for the alignment.

5. Experimental Study

Several experiments have been conducted in order to evaluate the performance of the proposed algorithm using different data sets. They are namely “St. Lucia” [36], “Nordland" [37], and the “Garden point" dataset. We compare the performance of the proposed algorithm with two of

the recent similar works, they are SVM and ABLE in particular. Besides, the LDB, SIFT, and HOG handcrafted features are used in these experiments.

5.1. Datasets and Evaluation

The “St. Lucia" dataset has been recorded using a webcam that is fixed to a car along a selected route across the St. Lucia suburb. The dataset was collected during ten runs. The route was visited five times in the early morning and the afternoon to show the difference in appearance. The same visits are repeated later after two weeks.

The Nordland dataset contains four video sequences each of which is recorded using a camera fixed to a train during its 10 hours trip during a train journey in a different season. Garden point dataset consists of three series of images collected at the Queensland campus. Two of the series (Day Left and Day Right) were collected at day, but with slightly different viewpoint, the third one (Night Right) collected at night with the same pose of the (Day Right). Each of these series consists of 200 images where the labels of images represent the correspondence between the series.

The performance of our proposed DTW algorithm is analyzed and quantified using the precision-recall curve (PRC). The curve is obtained after finding the best matches between the current and reference sequence, and then calculate the number of true positives, false positives, and false negatives. Then, the precision is according to

$$P = \frac{TP}{TP+FP}, \tag{6}$$

and the recall value is given as

$$R = \frac{TP}{TP+FN}. \tag{7}$$

In our analysis, a positive match is considered when the distance $D(\mathrm{i},\mathrm{j})$ is smaller than a given threshold t. If the distance is larger, we consider the match as a negative match.

5.2. Experiments and Results Analysis

In the following subsections we present our experiments outcomes. The three algorithms, i.e. DTW, ABLE and the SVM are evaluated using three types of features which are the HOG, SIFT, and LDB binary features. In these experiments, we have resized the image frames to a single unified dimensions. The size of the grid of HOG feature descriptor is set to 32 x 32, while a 128 bins are used for representing SIFT descriptor and a total of 40 SIFT features points are extracted. In addition, the OpenCV library was used to implement DTW and HOG, SIFT descriptors with python programming language. The source code provided by OpenABLE [1] was used to obtain the LDB features.

5.3. Experiments using “Nordland” Dataset

We present in this section the experimentation using the “Nordland" dataset, where the “Summer” and “Winter” sequences were used in these experiments. Two experiments were mainly conducted using this dataset.

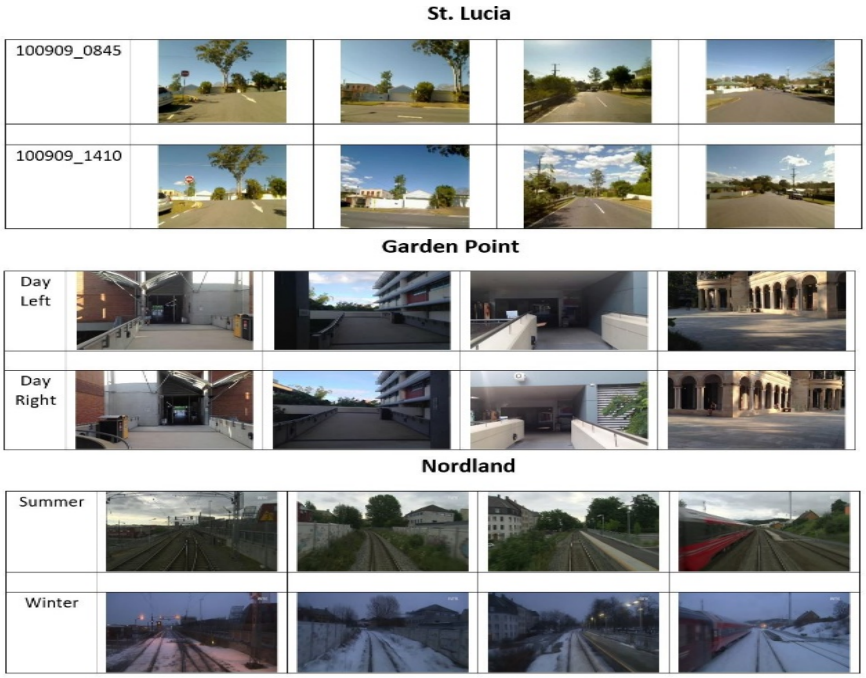

Fig. 3. Examples of pair images from the three datasets used in our experimentation. They are the “St. Lucia”, “Garden point", and “Nordland" datasets from top down.

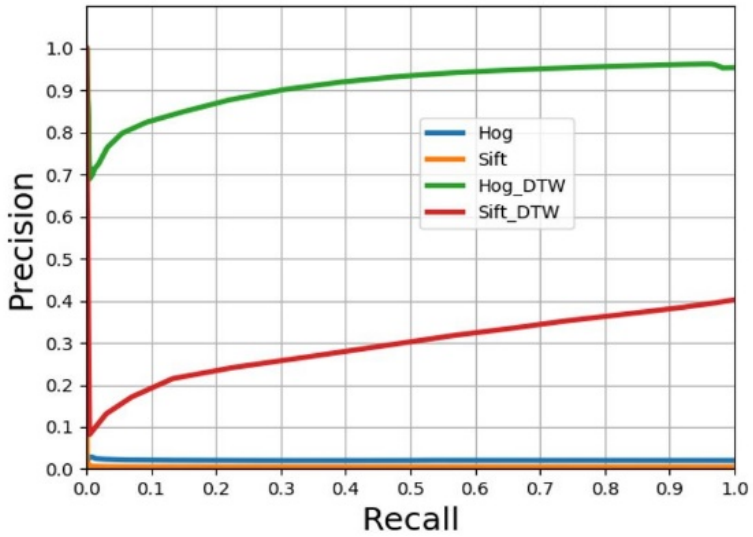

Fig. 4. Using the “Nordland" Dataset, the performance of HOG and SIFT using a nearest neighbor model is compared to the one using the, HOG-DTW and SIFT-DTW, i.e. using the proposed DTW. The precision-recall curve is used to quantify the performance.

5.3.1. Experiment 1

The performance of using the DTW algorithm along with HOG and SIFT was explored in this experiment using the “Nordland" dataset. The PRC is found using SIFT and HOG in a nearest neighbor model. In other words the best similar HOG or SIFT feature vector is used to classify the image from the test sequence to its matching frame from the reference sequence. After that the curve is found by applying the DTW to the image sequences represented by the HOG and the SIFT descriptors. Fig. 4 shows these PRCs.

As shown in Fig. 4, using the DTW algorithm has shown higher precision values for all recall values. The threshold between true or false positive matches is set to 1 frame.

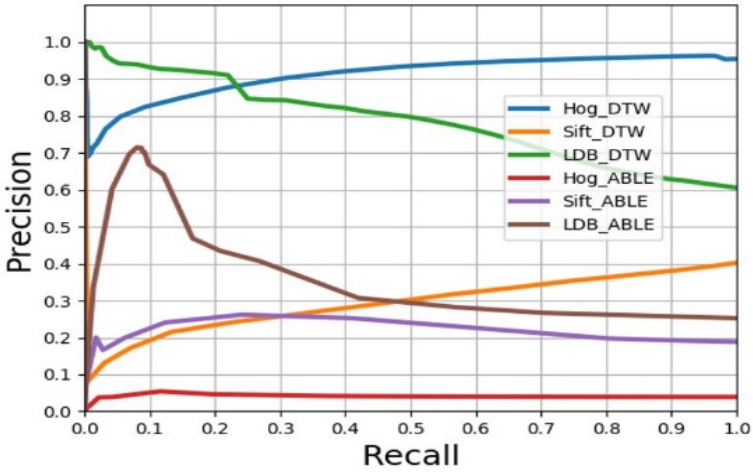

Fig. 5. Using the "Nordland" Dataset, the performance of DTW and ABLE algorithms is compared using the three types of features, HOG, SIFT, and LDB. The precision-recall curves is used to quantify the performance.

5.3.2. Experiment 2

The second experiment evaluates the performance of our proposal with respect to the ABLE algorithm using this "Nordland" dataset. As depicted in Fig. 5, both the HOG and LDB features using the proposed DTW (in green and blue) have outperformed the SIFT features, and also outperformed the same features using the ABLE algorithm. However, the HOG features have shown higher precision value for medium and higher recall values.

5.4. Experiments using "St. Lucia" Dataset

The experiments in this section are carried out using the "St. Lucia" dataset. The reference sequence was recorded at 8:45 o'clock morning, while the test sequence was recorded at the afternoon from the same day. Since the frames are tagged with its GPS coordinates values, a 15 meters threshold is selected to discriminate true positive matches from false positive ones.

Two experiments have been conducted using this dataset. The performance of the DTW algorithm is compared to the one of the ABLE algorithm and the SVM one.

5.4.1. Experiment 1: DTW vs. ABLE

The precision-recall curves resulted from these comparison with ABLE algorithm are shown in Fig. 6. The figure shows that the ABLE algorithm has resulted with a lower precision, regardless the recall values is large or small. This low precision has been observed for the different three feature descriptors. Besides, the precision of DTW while using the SIFT descriptor was small as well. The proposed DTW algorithm has shown a meaningfully higher precision for both descriptors HOG and LDB.

5.4.2. Experiment 2: DTW vs. SVM

Fig. 7 shows the comparison with SVM. The Figure shows lower precision using SVM algorithm. While the precision of DTW with SIFT descriptor was low, it achieved a

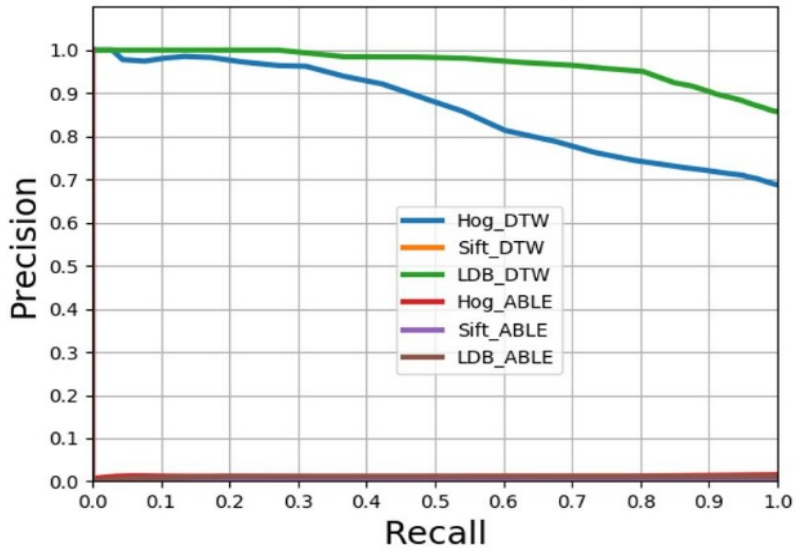

Fig. 6. Using the “St. Lucia" dataset, the performance of DTW and ABLE algorithms is compared using the three types of features, HOG, SIFT, and LDB. The precision-recall curves is used to quantify the performance.

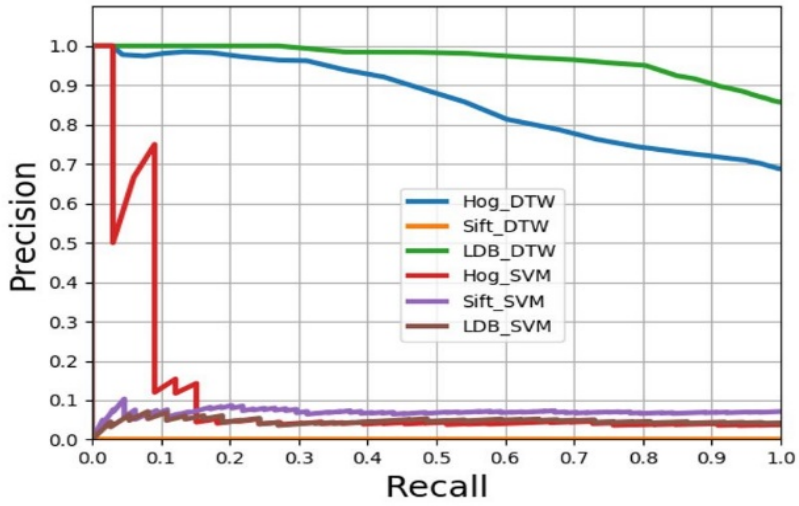

Fig. 7. Using the “St. Lucia" dataset, the performance of DTW and SVM algorithms is compared using the three types of features, HOG, SIFT, and LDB. The precision-recall curves is used to quantify the performance.

significantly higher precision for both HOG and LDB descriptors. It can be concluded that DTW with HOG and LDB has the best results.

5.5. Experiments using “Garden point” Dataset

The performance of our algorithm is compared to both ABLE and SVM algorithms using the “Garden point" dataset. The performance is quantified in the form of the precision-recall curve as depicted in Fig. 8 for comparison with ABLE and in Fig. 9 for comparison with SVM.

Similar to the case with “St. Lucia" dataset, the proposed DTW algorithm has outperformed both the ABLE and SVM algorithms, as depicted in Fig. 8 and Fig. 9 respectively. In these two figures, the precision-recall curve shows higher precision using the proposed DTW algorithm for all recall values. It is worth to notice that DTW has resulted with relatively lower precision values using the “Garden point" dataset than the case of using the “St. Lucia" dataset. This is

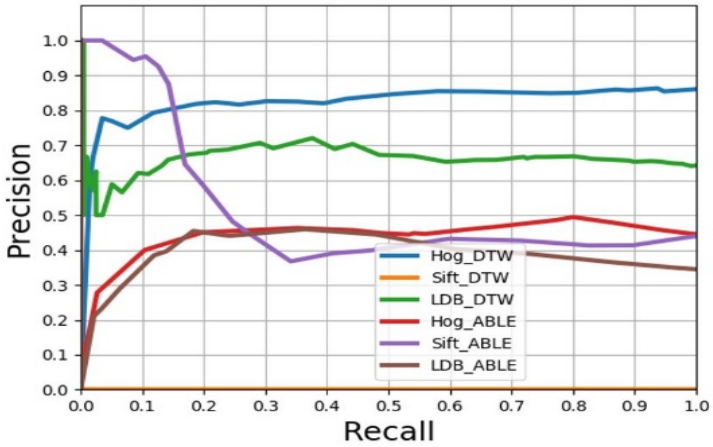

Fig. 8. Using the “Garden point" dataset, the performance of DTW and ABLE algorithms is compared using the three types of features, HOG, SIFT, and LDB. The precision-recall curves is used to quantify the performance.

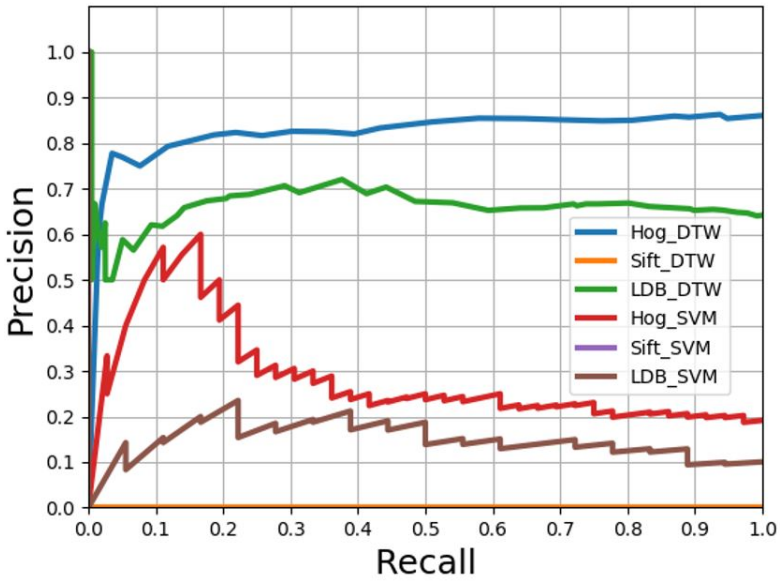

Fig. 9. Using the “Garden point" dataset, the performance of DTW and SVM algorithms is compared using the three types of features, HOG, SIFT, and LDB. The precision-recall curves are used to quantify the performance.

due to the nature of the “Garden point" dataset since it is highly textured comparing to the `St. Lucia" dataset. In addition to the different in pose and illumination between the test and reference sequences.

6. Conclusion Remarks

The dynamic programming based DTW algorithm is used here to perform visual localization of an autonomous agent. The basic idea of the contribution in this paper is to achieve a visual localization by aligning the pre-knowledge of the agent about the environment, i.e. stored in the form of a previously observed sequence of images, to the currently observed sequence of images.

The matching is achieved by dynamic time warping. The evaluation results have shown higher precision values for most of the recall values while using the proposed DTW algorithm. This proves the superiority of it with respect to the ABLE and SVM algorithms.

We plan to explore deep learning features with the proposed algorithm. In addition, a future work may include the introduction of encoding stage to reduce the complexity of the cost matrix calculation. Fisher vectors may help in reducing the dimensionality of the feature vector and also may eliminate the calculation of the complete cost matrix.

References

[1] Milford, M. J., and Wyeth G. F., SeqSLAM: Visual route-based navigation for sunny summer days and stormy winter nights, *IEEE International Conference on Robotics and Automation*, 1643-1649, 2012.

[2] Hafez, A. H., Agarwal, N. and Jawahar, C. V. Connecting Visual Experiences using Max-flow Network with Application to Visual Localization, *arXiv preprint arXiv:1808.00208*, 2018.

[3] Hafez, A. H., Arora, M., Krishna, K. M., and Jawahar, C. V., Learning multiple experiences useful visual features for active maps localization in crowded environments, *Advanced Robotics,* 30, 50-67, 2016.

[4] Hafez, A. H., Bhuvanagiri, S., Krishna, K. M., and Jawahar, C. V., On-line convex optimization based solution for mapping in VSLAM, *IEEE/RSJ International Conference on Intelligent Robots and Systems*, 4072-4077, 2008.

[5] Glover, A., Maddern, W., Warren, M., Reid, S., Milford, M. and Wyeth, G. F., OpenFABMAP: An open source toolbox for appearance-based loop closure detection, *IEEE International Conference on Robotics and Automation*, 4730-4735, 2012.

[6] Naseer, T., Burgard, W., and Stachniss, C., Robust visual localization across seasons, *IEEE Transactions on Robotics,* 34, 289-302, 2018.

[7] Arroyo, R., Alcantarilla, P.F., Bergasa, L.M., Yebes, J.J. and Gámez, S., Bidirectional loop closure detection on panoramas for visual navigation, *IEEE Intelligent Vehicles Symposium Proceedings*, 1378-1383, 2014.

[8] Garcia-Fidalgo, E. and Ortiz, A., Methods for Appearance-based Loop Closure Detection, *Springer International Publishing*, 1st Edition, 2018.

[9] Hafez, A. H., Singh, M., Krishna, K.M. and Jawahar, C.V., Visual localization in highly crowded urban environments, *IEEE/RSJ International Conference on Intelligent Robots and Systems*, 2778-2783, 2013.

[10] Hafez, A.H., Arora, M., Krishna, K.M. and Jawahar, C.V., Learning multiple experiences useful visual features for active maps localization in crowded environments, *Advanced Robotics,* 30, 50-67, 2016.

[11] Murphy, L., Martin, S. and Corke, P., Creating and using probabilistic costmaps from vehicle experience, *IEEE/RSJ International Conference on Intelligent Robots and Systems*, 4689-4694, 2012.

[12] Churchill, W. and Newman, P., Experience-based navigation for long-term localization, *The International Journal of Robotics Research,* 32,1645-1661, 2013.

[13] Dymczyk, M., Lynen, S., Cieslewski, T., Bosse, M., Siegwart, R. and Furgale, P., The gist of maps-summarizing experience for lifelong localization, *IEEE International Conference on Robotics and Automation (ICRA)*, 2767-2773, 2015.

[14] Labbé, M. and Michaud, F., Memory management for real-time appearance-based loop closure detection, *IEEE/RSJ international conference on intelligent robots and systems*, 1271-1276, 2011.
[15] Labbe, M. and Michaud, F., Appearance-based loop closure detection for online large-scale and long-term operation, *IEEE Transactions on Robotics,* 29, 734-745, 2013.
[16] Cummins, M. and Newman, P., FAB-MAP: Probabilistic localization and mapping in the space of appearance, *The International Journal of Robotics Research,* 27, 647-665, 2008.
[17] Schindler, G., Brown, M. and Szeliski, R., City-scale location recognition, *IEEE Conference on Computer Vision and Pattern Recognition*, 1-7, 2007.
[18] Dymczyk, M., Lynen, S., Cieslewski, T., Bosse, M., Siegwart, R. and Furgale, P., The gist of maps-summarizing experience for lifelong localization, *IEEE International Conference on Robotics and Automation (ICRA)*, 2767-2773, 2015.
[19] Zeng, F., Jacobson, A., Smith, D., Boswell, N., Peynot, T. and Milford, M., Enhancing underground visual place recognition with shannon entropy saliency, *Proceedings of the Australasian Conference on Robotics and Automation 2017*, 1-10, 2017.
[20] Abbas M Ali and Tarik A Rashid., Place recognition using kernel visual keyword descriptors, *SAI Intelligent Systems Conference (IntelliSys)*, 921–926, 2015.
[21] Qiao, Y., Cappelle, C. and Ruichek, Y., Place recognition based visual localization using LBP feature and SVM, *Mexican International Conference on Artificial Intelligence*, 393-404, 2015.
[22] Bellman, R., Some applications of the theory of dynamic programming—a review, *Journal of the Operations Research Society of America*, 2, 275–288, 1954.
[23] Myers, C., Rabiner, L. and Rosenberg, A., Performance tradeoffs in dynamic time warping algorithms for isolated word recognition, *IEEE Transactions on Acoustics*, Speech, and Signal Processing, 28, 623–635, 1980.
[24] Sakoe, H. and Chiba, S., Dynamic programming algorithm optimization for spoken word recognition, *IEEE transactions on acoustics*, speech, and signal processing, 26, 43–49, 1978.
[25] Efrat, A., Fan, Q. and Venkatasubramanian, S., Curve matching, time warping, and light fields: New algorithms for computing similarity between curves, *Journal of Mathematical Imaging and Vision*, 27, 203–216, 2007.
[26] Charles C. Tappert, Ching Y. Suen, and Toru Wakahara., The state of the art in online handwriting recognition, *IEEE Transactions on pattern analysis and machine intelligence*, 12, 787–808, 1990.
[27] Kuzmanic, A. and Zanchi, V., Hand shape classification using dtw and lcss as similarity measures for vision-based gesture recognition system, *EUROCON 2007-The International Conference on Computer as a Tool*, 264–269, 2007.
[28] Niennattrakul, V. and Ratanamahatana, C.A., On clustering multimedia time series data using k-means and dynamic time warping, *International Conference on Multimedia and Ubiquitous Engineering (MUE'07)*, 733–738, 2007.
[29] Gu, J. and Jin, X., A simple approximation for dynamic time warping search in large time series database, *International Conference on Intelligent Data Engineering and Automated Learning*, 841– 848, 2006.
[30] Müller, M., Dtw-based motion comparison and retrieval. *Information Retrieval for Music and Motion*, 211–226, 2007.
[31] Zhang, Z., Huang, K. and Tan, T., Comparison of similarity measures for trajectory clustering in outdoor surveillance scenes, *18th International Conference on Pattern Recognition (ICPR'06)*, 3, 1135-1138, 2006.
[32] Vial, J., Noçairi, H., Sassiat, P., Mallipatu, S., Cognon, G., Thiébaut, D., Teillet, B. and Rutledge, D.N., Combination of dynamic time warping and multivariate analysis for the

comparison of comprehensive two-dimensional gas chromatograms: application to plant extracts, *Journal of Chromatography A*, 1216, 2866–2872, 2009.
[33] Müller, M., Mattes, H. and Kurth, F., An efficient multiscale approach to audio synchronization, *In ISMIR*, 546, 192–197, 2006.
[34] Kate, R.J., Using dynamic time warping distances as features for improved time series classification, *Data Mining and Knowledge Discovery*, 30, 283–312, 2016.
[35] Petitjean, F., Forestier, G., Webb, G.I., Nicholson, A.E., Chen, Y. and Keogh, E., Faster and more accurate classification of time series by exploiting a novel dynamic time warping averaging algorithm, *Knowledge and Information Systems*, 47, 1–26, 2016.
[36] Glover, A.J., Maddern, W.P., Milford, M.J. and Wyeth, G.F., FAB-MAP+ RatSLAM: Appearance-based SLAM for multiple times of day, *IEEE international conference on robotics and automation*, 3507-3512, 2010.
[37] Olid, D., Fácil, J.M. and Civera, J., Single-view place recognition under seasonal changes, *PPNIV Workshop at IROS 2018*, 2018.

International Journal of Engineering & Applied Sciences (IJEAS)
Vol. 12, Issue 1 (2020) 15-31
http://dx.doi.org/10.24107/ijeas.714965
Int J Eng Appl Sci 12(1) (2020) 15-31

Numerical Solutions of Second Order Initial Value Problems of Bratu-Type Equations using Predictor-Corrector Method

Mengistu Mekonnen [a], Genanew Gofe [b], Habtamu Garoma [c,]*

[a,c] Department of Mathematics, Jimma University, Jimma, P. O. Box 378, ETHIOPIA

[b]Department of Mathematics, Salale University, Fiche, P. O. Box 245, ETHIOPIA
[*]E-mail address: manmak556@gmail.com, genagof@gmail.com, habte200@gmail.com[*]

ORCID numbers of authors:
0000-0001-6338-4433, 0000-0001-7278-5730, 0000-0003-1033-3602[*]

Received date: 05.04.2020
Accepted date: 23.04.2020

Abstract

In this paper, numerical solutions of second order initial value problems of Bratu-type equation using predictor-corrector method is considered. The stability and convergence analysis are investigated. To validate the applicability of the scheme, two model problems are considered for numerical experimentation. In a nutshell, the present method improves the findings of some existing numerical methods reported in the literature.

Keywords: Predictor-corrector method, Initial value problem, quasi linearization method, Bratu-Type equation

1. Introduction

In this paper we presented a problem of the form

$$u''(x) + \lambda e^{u(x)} = 0, \quad 0 \le x \le l \tag{1}$$

subject to the initial conditions

$$u(0) = \alpha, \;\; u'(0) = \gamma \tag{2}$$

where λ, α and γ are constant numbers for $u(x)$ is unknown function.
In numerical analysis, predictor-corrector methods belong to a class of algorithms designed to integrate ordinary differential equations to find an unknown function that satisfies a given differential equation. When considering the numerical solution of ordinary differential equations (ODEs), a predictor-corrector method typically uses an explicit method for the predictor step and an implicit method for the corrector step. Bratu-Type equation is widely used in science and engineering to describe complicated physical and chemical models [1]. As author [2] stated, recently much attention has been given to develop several iterative methods for solving nonlinear equations of Bratu-type of equations. The nonlinear models of real-life problems are still difficult to solve analytically. Authors [3], [4] said that there has been recently much attention devoted to the search for better and more efficient numerical methods for determining a solution to nonlinear models. Recently, authors [5-9] solves Bratu type equation using different numerical method but still there is a room for accuracy of the governing problem under consideration. Therefore, it is important to develop more accurate and convergent numerical method for solving second order Bratu-type equation. Thus, the purpose of this study is to develop stable, convergent and more accurate numerical method for solving initial value problems of Bratu-Type equations. We first linearize the given equation using quasi-linearization formula and then used fourth order Adams-Bash forth method as a predictor and Adams-Moulton fourth order method as a corrector. The starting values (u_1, u_2, u_3) were calculated using Runge-Kutta fourth order method.

2. Formulation of the method

Bratu-type of Eq. (1) can be transformed to a linear differential problem using the quasi linearization method and we get the iterative scheme as

$$u''_{k+1}(x) + \lambda e^{u_k(x)} + u'_{k+1}(x) = \lambda e^{u_k(x)}(u_k(x) - 1) \tag{3}$$

with initial condition

$$u_{k+1}(0) = \beta \text{ and } u'_{k+1}(0) = \gamma \tag{4}$$

where $k = 1, 2, 3, ...$
Eq. (3) can be used to compute $u_{k+1}(x)$ provided $u_k(x)$ is known. In particular, the initial approximation $u_0(x)$ must be specified so that we compute $u_1(x)$. Once $u_1(x)$ is known, we compute $u_2(x)$ using Eq. (3) and so on.
Eqs. (3) and (4) can be reduced to the equations

$$Lu \equiv u''(x) + a(x)u(x) = b(x), \quad 0 \le x \le l, \tag{5}$$

$$\text{where, } a(x) = \lambda e^{u(x)} \text{ and } b(x) = \lambda e^{u(x)}(u(x) - 1)$$

with initial condition

$$u(0) = \alpha \text{ and } u'(0) = \gamma \tag{6}$$

Therefore, the given second order IVP of Bratu equation is linearized to Eq. (5) with initial condition (6) can be solved by explicit-implicit Adams-Bashforth-Moulton predictor-corrector method. Eq. (5) can be reduced to first order system of equations using the substitutions $v(x) = u'(x)$ and $v'(x) = u''(x)$. Then Eq. (5) and Eq. (6) can be re-written as:

$$\begin{cases} u'(x) = v(x) = F(x,u,v), & u(0) = \alpha \\ v'(x) = b(x) - a(x)u(x) = G(x,u,v), & v(0) = \gamma \end{cases} \tag{7}$$

Dividing the interval $[0, l]$ into N equal subinterval of mesh length h and the mesh point is given by $x_n = x_0 + nh$, for $n = 1,2,...,N-1$. For the sake of simplicity let use the notation: $u(x_n) = u_n$, $v(x_n) = v_n$, etc. Thus, at the nodal point x_n Eq. (7), written as:

$$\begin{cases} u_n' = F(x_n,u_n,v_n), & u(0) = \alpha \\ v_n' = G(x_n,u_n,v_n), & v(0) = \gamma \end{cases} \tag{8}$$

where $G(x_n,u_n,v_n) = -a(x_n)u(x_n) + b(x_n)$

To solve the system of equations given in Eq. (8), we use explicit-implicit multi step methods that require information about the solution at x_n to calculate at x_{n+1} from the solution at a number of previous solutions using Runge-Kutta method as self-starter.

For the general case let's consider the first order nonlinear equal spaced initial value problem (IVP) of the form

$$u'(x) = f(x,u(x)), \quad u(x_0) = \alpha \tag{9}$$

The IVP of the form of Eq. (9) can be solved by using fourth order Runge-Kutta method. The general fourth order Runge-Kutta method of Eq. (9) is given by [10].

$$u_{n+1} = u_n + h\sum_{n=1}^{4} w_n k_n \tag{10}$$

where $k_n = f(x_n + c_n h,\ u_n + \sum_{j=1}^{4} a_{n,j} k_j)$

For particular fourth order classical Runge-Kutta method we have:

$$u_{n+1} = u_n + \frac{1}{6} h(k_1 + 2k_2 + 2k_3 + k_4) \tag{11}$$

where $k_1 = f(x_n, u_n),\ \ k_2 = f(x_n + \frac{1}{2}h, u_n + \frac{1}{2}k_1),\ \ \ k_3 = f(x_n + \frac{1}{2}h, u_n + \frac{1}{2}k_2)$

$k_4 = f(x_n + h, u_n + k_3)$

For the fourth order Runge-Kutta method of the system of equations of the form of Eq. (8) can also be expressed as:

$$\begin{cases} u_{n+1} = u_n + \sum_{n=1}^{4} w_n k_n \\ v_{n+1} = v_n + \sum_{n=1}^{4} w_n k_n \end{cases} \tag{12}$$

where $\begin{cases} k_n = hF(x_n + c_n h,\ u_n + \sum_{j=1}^{4} a_{nj} k_j,\ v_n + \sum_{j=1}^{4} a_{nj} m_j) \\ m_n = hG(x_n + c_n h,\ u_n + \sum_{j=1}^{4} a_{nj} k_j,\ v_n + \sum_{j=1}^{4} a_{nj} m_j) \end{cases}$

Eq. (12) can also be simplified to the fourth order of classical Runge-Kutta method as:

$$\begin{cases} u_{n+1} = u_n + \frac{1}{6} h(k_1 + 2k_2 + 2k_3 + k_4) \\ v_{n+1} = v_n + \frac{1}{6} h(m_1 + 2m_2 + 2m_3 + m_4) \end{cases} \tag{13}$$

where

$$k_1 = F(x_n, u_n, v_n) \qquad m_1 = G(x_n, u_n, v_n)$$
$$k_2 = F(x_n + \frac{1}{2}h, u_n + \frac{1}{2}k_1, v_n + \frac{1}{2}m_1) \qquad m_2 = G(x_n + \frac{1}{2}h, u_n + \frac{1}{2}k_1, v_n + \frac{1}{2}m_1)$$
$$k_3 = F(x_n + \frac{1}{2}h, u_n + \frac{1}{2}k_2, v_n + \frac{1}{2}m_2) \qquad m_3 = G(x_n + \frac{1}{2}h, u_n + \frac{1}{2}k_2, v_n + \frac{1}{2}m_2)$$
$$k_4 = F(x_n + h, u_n + k_3, v_n + m_3) \qquad m_4 = G(x_n + h, u_n + k_3, v_n + m_3)$$

Using Eq. (13) we can derive the general formula of the linearized Bratu equation of Eq. (8). Let calculate the values of k_i and m_i for $i = 1, 2, 3$ and 4 as follow:

$$k_1 = F(x_n, u_n, v_n) = u_n^{'}$$
$$m_1 = G(x_n, u_n, v_n) = -a_n u_n + b_n$$

$$k_2 = F(x_n + \frac{1}{2}h, u_n + \frac{1}{2}k_1, v_n + \frac{1}{2}m_1) \qquad m_2 = G(x_n + \frac{1}{2}h, u_n + \frac{1}{2}k_1, v_n + \frac{1}{2}m_1)$$
$$= u_n' + \frac{1}{2}u_n'' \qquad = -a_n(u_n + \frac{1}{2}u_n') + b_n$$

$$k_3 = F(x_n + \frac{1}{2}h, u_n + \frac{1}{2}k_2, v_n + \frac{1}{2}m_2) \qquad m_3 = G(x_n + \frac{1}{2}h, u_n + \frac{1}{2}k_2, v_n + \frac{1}{2}m_2)$$
$$= u_n' + \frac{1}{2}u_n'' + \frac{1}{4}u''' \qquad = -a_n(u_n + \frac{1}{2}u_n' + \frac{1}{4}u_n'') + b_n$$

$$k_4 = F(x_n + h, u_n + k_3, v_n + m_3) \qquad m_4 = G(x_n + h, u_n + k_3, v_n + m_3)$$
$$= u_n' + u_n'' + \frac{1}{2}u''' + \frac{1}{4}u_n^{(4)} \qquad = -a_n(u_n + u_n' + \frac{1}{2}u_n'' + \frac{1}{4}u''') + b_n$$

Using Eq. (13) we can derive the general formula of the linearized Bratu equation of Eq. (8). Let calculate the values of k_i and m_i for $i = 1, 2, 3$ and 4 as follow:

$$k_1 = F(x_n, u_n, v_n) = u_n^{'}$$
$$m_1 = G(x_n, u_n, v_n) = -a_n u_n + b_n$$

$$k_2 = F(x_n + \frac{1}{2}h, u_n + \frac{1}{2}k_1, v_n + \frac{1}{2}m_1) \qquad m_2 = G(x_n + \frac{1}{2}h, u_n + \frac{1}{2}k_1, v_n + \frac{1}{2}m_1)$$
$$= u_n' + \frac{1}{2}u_n'' \qquad = -a_n(u_n + \frac{1}{2}u_n') + b_n$$

$$k_3 = F(x_n + \frac{1}{2}h, u_n + \frac{1}{2}k_2, v_n + \frac{1}{2}m_2) \qquad m_3 = G(x_n + \frac{1}{2}h, u_n + \frac{1}{2}k_2, v_n + \frac{1}{2}m_2)$$
$$= u_n' + \frac{1}{2}u_n'' + \frac{1}{4}u''' \qquad = -a_n(u_n + \frac{1}{2}u_n' + \frac{1}{4}u_n'') + b_n$$

$$k_4 = F(x_n + h, u_n + k_3, v_n + m_3) \qquad m_4 = G(x_n + h, u_n + k_3, v_n + m_3)$$
$$= u_n' + u_n'' + \frac{1}{2}u''' + \frac{1}{4}u_n^{(4)} \qquad = -a_n(u_n + u_n' + \frac{1}{2}u_n'' + \frac{1}{4}u''') + b_n$$

Then substituting these values of k_i's and m_i's $(\mathrm{i} = 1, 2, 3, 4)$ in Eq. (13) and simplifying the equations separately for u_{n+1} and v_{n+1} we get:

$$\begin{aligned} u_{n+1} &= u_n + \frac{1}{6}h(k_1 + 2k_2 + 2k_3 + k_4) \\ &= u_n + h(u_n' + \frac{1}{2}u_n'' + \frac{1}{6}u''' + \frac{1}{24}u_n^{(4)}) \end{aligned} \tag{14}$$

and the values of v_{n+1} can also be calculated as follows:

$$\begin{aligned} v_{n+1} &= v_n + \frac{1}{6}h(m_1 + 2m_2 + 2m_3 + m_4) \\ &= v_n - h(a_n u_n + \frac{1}{2}a_n u_n' + \frac{1}{6}a_n u_n'' + \frac{1}{24}a_n u_n''' + b_n) \end{aligned} \tag{15}$$

Therefore the system of equation (13) simplified to:

$$\begin{cases} u_{n+1} = u_n + h(u_n' + \frac{1}{2}u_n'' + \frac{1}{6}u_n''' + \frac{1}{24}u_n^{(4)}) \\ v_{n+1} = v_n - h(a_n u_n + \frac{1}{2}a_n u_n' + \frac{1}{6}a_n u_n'' + \frac{1}{24}a_n u_n''' + b_n) \end{cases} \tag{16}$$

This equation is Runge-Kutta fourth order formula used to approximate the values of u_n and v_n for $\mathrm{n} = 1, 2, 3$ since the Adams-Bashforth-Moulton predictor-corrector method requires these values.

To solve Eq. (9), we can apply the explicit-implicit multistep method that requires information about the solution at x_{n+1} from the solution at a number of previous solutions.

To begin the derivation of the multi-step methods, if we integrate the initial-value problem over the interval $[x_n, x_{n+1}]$, then the following property exists:

$$u(x_{n+1}) = u(x_n) + \int_{x_n}^{x_{n+1}} f(x, u(x))dx \tag{17}$$

where $f(x,u(x))$ is the first derivative of $u(x)$. To derive an Adams-Bashforth method, Newton backward difference formula with a set of equal spacing points, x_{n+1-k}, ..., x_{n-1}, x_n, is used to approximate the integral and the fourth order Adams-Bashforth method is given by [2].

$$u_{n+1} = u_n + \frac{h}{24}\left[55f_n - 59f_{n-1} + 37f_{n-2} - 9f_{n-3}\right] + T_k \tag{18}$$

where, T_k is the truncation error of the fourth order Adams-Bashforth method and is given by:

$$T_k = \frac{251}{720}h^5 u^{(5)}(\xi) = O(h^5) \tag{19}$$

To use Eq. (18), we require the starting values u_n, u_{n-1}, u_{n-2} and u_{n-3} which are calculated by self-starting single step method, Runge-Kutta fourth order method for our case. The fourth order Adams-Bashforth method for the system of Eq. (8), can be solved using Eq. (18) and it becomes

$$\begin{cases} u_{n+1} = u_n + \frac{h}{24}\left[55F_n - 59F_{n-1} + 37F_{n-2} - 9F_{n-3}\right] \\ v_{n+1} = v_n + \frac{h}{24}\left[55G_n - 59G_{n-1} + 37G_{n-2} - 9G_{n-3}\right] \end{cases} \tag{20}$$

Using Eq. (20) we can formulate the general form of the systems of Eq. (8) for $n \geq 4$. Therefore, Eq. (20) can be derived as follow:

$$u_{n+1} = u_n + \frac{h}{24}(55F_n - 59F_{n-1} + 37F_{n-2} - 9F_{n-3}) \tag{21}$$

But, since the values of F_n, F_{n-1}, F_{n-2} and F_{n-3}, for $n \geq 4$, can be calculated using the linearized system of Eq. (8), we have

$$F_n = u'_n,\ F_{n-1} = u'_{n-1},\ F_{n-2} = u'_{n-2},\ F_{n-3} = u'_{n-3}, \tag{22}$$

Then

$$u_{n+1} = u_n + \frac{h}{24}(55u'_n - 59u'_{n-1} + 37u'_{n-2} - 9u'_{n-3}) \tag{23}$$

For

$$v_{n+1} = v_n + \frac{h}{24}(55G_n - 59G_{n-1} + 37G_{n-2} - 9G_{n-3}) \tag{24}$$

where the values of $G_n,\ G_{n-1}, G_{n-2}, G_{n-3}$ are given by:

$$\begin{cases} G_n = -a_n u_n + b_n, \quad G_{n-1} = -a_{n-1}u_{n-1} + b_{n-1}, \\ G_{n-2} = -a_{n-2}u_{n-2} + b_{n-2}, \quad G_{n-3} = -a_{n-3}u_{n-3} + b_{n-3} \end{cases} \tag{25}$$

So, Eq. (24) becomes

$$\begin{aligned} v_{n+1} = v_n + \frac{h}{24}(&55(-a_n u_n + b_n) - 59(-a_{n-1}u_{n-1} + b_{n-1}) + 37(-a_{n-2}u_{n-2} + b_{n-2}) \\ &- 9(-a_{n-3}u_{n-3} + b_{n-3})) \end{aligned} \tag{26}$$

Then summarizing Eq. (23) and (26), we have

$$\begin{cases} u_{n+1} = u_n + \dfrac{h}{24}(55u'_n - 59u'_{n-1} + 37u'_{n-2} - 9u'_{n-3}) \\ v_{n+1} = v_n + \dfrac{h}{24}(55(-a_n u_n + b_n) - 59(-a_{n-1}u_{n-1} + b_{n-1}) + 37(-a_{n-2}u_{n-2} + b_{n-2}) \\ \qquad\qquad - 9(-a_{n-3}u_{n-3} + b_{n-3})) \end{cases} \tag{27}$$

Therefore, Eq. (27) is the fourth order Adams-Bashforth predictor method for the given system of Eq. (8).

Similarly, to solve the given nonlinear differential equation using fourth order Adams-Moulton method, first let's consider the first order nonlinear IVP of the form Eq. (9) and the method is derived by using the set of equal spacing points, $x_{n+2-k}, ..., x_n, x_{n+1}$.
Integrating both sides of Eq. (9) with respect to x from x_n to x_{n+1} we have,

$$u(x_{n+1}) = u(x)_n + \int_{x_n}^{x_{n+1}} f(x,u(x))dx \tag{28}$$

Replace $f(x,u)$ of Eq. (27) by the polynomial $p_k(x)$ of degree k, which interpolates $f(x,u)$ at $k+1$ points and Newton backward interpolation formula, gives polynomial of degree k and the fourth order Adams-Moulton method is given by:

$$u_{n+1} = u_n + \frac{h}{24}\left[9f_{n+1} + 19f_n - 5f_{n-1} + f_{n-2}\right] + T_l \tag{29}$$

where, the truncation error T_l is given by:

$$T(x) = \frac{-19}{720}h^5 u^{(5)}(\xi) = O(h^5) \tag{30}$$

The system of Eq. (8), is then given by

$$\begin{cases} u_{n+1} = u_n + \dfrac{h}{24}\left[9F_{n+1} + 19F_n - 5F_{n-1} + F_{n-2}\right] \\ v_{n+1} = v_n + \dfrac{h}{24}\left[9G_{n+1} + 19G_n - 5G_{n-1} + G_{n-2}\right] \end{cases} \tag{31}$$

To apply Eq. (31) on Bratu equation, we simplify this equation using the same procedures as we have done for the predictor (Adams-Bashforth method) above.

That is, the values of $F_{n+1}, F_n, F_{n-1}, F_{n-2}$ and $G_{n+1}, G_n, G_{n-1}, G_{n-2}$ are as calculated for the predictor method. Therefore, the system of Eq. (31) can be written as:

$$\begin{cases} u_{n+1} = u_n + \dfrac{h}{24}(9u'_{n+1} + 19u'_n - 5u'_{n-1} + u'_{n-2}) \\ v_{n+1} = v_n + \dfrac{h}{24}(9(-a_{n+1}u_{n+1} + b_{n+1}) + 19(-a_n u_n + b_n) - 5(-a_{n-1}u_{n-1} + b_{n-1}) \\ \qquad\qquad + (-a_{n-2}u_{n-2} + b_{n-2})) \end{cases} \tag{32}$$

This is the Adams-Moulton corrector formula. We use the fourth order Adams-Bashforth method as a predictor and Adams-Moulton method as a corrector and we have the following equations.

$$\begin{cases} u^p_{n+1} = u_n + \dfrac{h}{24}\left[55F_n - 59F_{n-1} + 37F_{n-2} - 9F_{n-3}\right] \\ v^p_{n+1} = v_n + \dfrac{h}{24}\left[55G_n - 59G_{n-1} + 37G_{n-2} - 9G_{n-3}\right] \end{cases} \tag{33}$$

where $F^*_{n+1} = F(x_{n+1}, u^p{}_{n+1}, v^p{}_{n+1})$

$G^*_{n+1} = G(x_{n+1}, u^p{}_{n+1}, v^p{}_{n+1})$

$$\begin{cases} y^c{}_{n+1} = y_n + \dfrac{h}{24}\left[9F^*{}_{n+1} + 19F_n - 5F_{n-1} + F_{n-2}\right] \\ z^c{}_{n+1} = z_n + \dfrac{h}{24}\left[9G^*{}_{n+1} + 19G_n - 5G_{n-1} + G_{n-2}\right] \end{cases} \tag{34}$$

u_{n+1}^{p} and v_{n+1}^{p} are calculated from Eq. (34) and applying these equations on the linearized Bratu equations is the same as combining Eq. (27) and Eq. (32), using Eq. (27) as a predictor and Eq.(32) as a corrector and it becomes:

Predictor Formula

$$\begin{cases} u_{n+1}^{p} = u_n + \dfrac{h}{24}(55u_n' - 59u_{n-1}' + 37u_{n-2}' - 9u_{n-3}') \\ v_{n+1}^{p} = v_n + \dfrac{h}{24}(55(-a_n u_n + b_n) - 59(-a_{n-1}u_{n-1} + b_{n-1}) + 37(-a_{n-2}u_{n-2} + b_{n-2}) \\ \qquad\qquad - 9(-a_{n-3}u_{n-3} + b_{n-3})) \end{cases} \tag{35}$$

and corrector formula

$$\begin{cases} u_{n+1}^{c} = u_n + \dfrac{h}{24}(9(u_{n+1}^{p})' + 19u_n' - 5u_{n-1}' + u_{n-2}') \\ v_{n+1}^{c} = v_n + \dfrac{h}{24}(9(-a_{n+1}u_{n+1}^{p} + b_{n+1}) + 19(-a_n u_n + b_n) - 5(-a_{n-1}u_{n-1} + b_{n-1}) \\ \qquad\qquad + (-a_{n-2}u_{n-2} + b_{n-2})) \end{cases} \tag{36}$$

3. Truncation Error, Convergence and Stability Analysis

Let's consider the more general multistep method of the following

$$\begin{aligned} &\frac{\left[U(t_{k+1}) + \alpha_1 U(t_k) + \alpha_2 U(t_{k-1}) + \ldots + \alpha_m U(t_{k+1-m})\right]}{h} \\ &= \beta_0 f(t_{k+1}, U(t_{k+1})) + \beta_1 f(t_k, U(t_k)) + \ldots + \beta_m f(t_{k+1-m}, U(t_{k+1-m})) \end{aligned} \tag{37}$$

where α_i and β_j, (for $i = 1, 2, 3, \ldots, m$ and $j = 1, 2, 3, \ldots, m$) are constants.

Theorem 1: If a sequence of numbers e_k satisfies

$$e_{k+1} + \rho_1 e_k + \rho_2 e_{k-1} + ... + \rho_m e_{k+1-m} = hT_k \tag{38}$$

for $k \geq m-1 (m \geq 1)$ and if all the roots of the corresponding characteristic polynomial

$$\lambda^m + \rho_1 \lambda^{m-1} + \rho_2 \lambda^{m-2} + ... + \rho_m \tag{39}$$

are less than or equal to one in absolute value, and all multiple roots are strictly less than one in absolute value, then

$|e_k| \leq M_\rho \left[\max\{|e_0|,...,|e_{m-1}|\} + t_k T\right]$, where $t_k = kh$, $T = \max|T_j|$, and M_ρ is a constant depending only on the ρ_i.

Definition: The *region of absolute stability* of a multistep method consists of those values of *ah* in the complex plane for which all roots of polynomial

$$(1-\beta_0 ah)\lambda^m + (\alpha_1 - \beta_1 ah)\lambda^{m-1} + (\alpha_2 - \beta_2 ah)\lambda^{m-2} + ... + (\alpha_m - \beta_m ah) \tag{40}$$

are less than or equal to one in absolute value, and all multiple roots are strictly less than one in absolute value.

Theorem 2: The multistep method (29) is stable provided all roots of

$$\lambda^m + \alpha_1 \lambda^{m-1} + \alpha_2 \lambda^{m-2} + ... + \alpha_m \tag{41}$$

are less than or equal to one in absolute value, and all multiple roots are strictly less than one in absolute value.

The error terms for the numerical integration formulas used to obtain both the predictor and corrector are of the order $O(h^5)$. Therefore, the local truncation errors of predictor and corrector are respectively

$$\begin{cases} u(t_{n+1}) - p_{n+1} = \dfrac{251}{720} h^5 u^{(5)}(\xi) \\ u(t_{n+1}) - u_{n+1} = \dfrac{-19}{720} h^5 u^{(5)}(\xi) \end{cases} \tag{42}$$

where $u(t_{n+1})$ is given by Eq. (15) for the predictor and Eq. (20) for corrector and p_{n+1} and u_{n+1} are calculated values for Adams-Bash forth predictor and Adams-Moulton corrector given by Eqs. (16) and (29) respectively

3. Stability Analysis

Some of the most popular higher-order, stable, multistep methods are the Adams methods, which ensure stability by choosing $\alpha_1 = -1$ and $\alpha_2 = \alpha_3 = ... = \alpha_m = 0$. The characteristic polynomial corresponding to theorem 1 is $\lambda^m - \lambda^{m-1}$ which has 1 as a simple root and 0 as a multiple root. Thus these methods are stable regardless of the values chosen for the β_i's.

The values of β_i's are determined in order to maximize the order of the truncation error. For Adams-Bashforth method we can calculate the value of β_i as [2]:

$$\begin{cases} \beta_0 = \int_0^1 (-1)^0 \binom{-s}{0} ds = 1, \ \beta_1 = \int_0^1 (-1)^1 \binom{-s}{1} ds = \dfrac{1}{2}, \ \beta_2 = \int_0^1 (-1)^2 \binom{-s}{2} ds = \dfrac{5}{12}, \\ \beta_3 = \int_0^1 (-1)^3 \binom{-s}{3} ds = \dfrac{3}{8}, \ \beta_4 = \int_0^1 (-1)^4 \binom{-s}{4} ds = \dfrac{251}{720} \end{cases} \tag{43}$$

And also for Adams-Moulton method we have

$$\beta_0 = 1, \ \beta_1 = -\frac{1}{2}, \ \beta_2 = -\frac{1}{12}, \ \beta_3 = -\frac{1}{24}, \ \beta_4 = -\frac{19}{720} \tag{44}$$

Since for all Adams methods the values of $\alpha_1 = -1$ and $\alpha_2 = \alpha_3 = ... = \alpha_m = 0$, the fourth order Adams-Bashforth method (Eq. 18) and fourth order Adams-Moulton method Eq. (31) have the characteristic equation of

$$\rho(\lambda) = \lambda^4 - \lambda^3 = 0 \Rightarrow \lambda^3(\lambda - 1) = 0 \tag{45}$$

$\Rightarrow \lambda = 1$ is a simple root and 0 is a multiple root with multiplicity 3.

Therefore, since the simple root is 1, and multiple roots are 0 which is strictly less than 1, by Theorem 1, Adams-Bash forth and Adams-Moulton methods are stable.

4. **Numerical Examples and Results**

To demonstrate the applicability of the method, we implemented the method on four numerical examples To show the applicability and efficiency of the method, we have taken two examples of Bratu-type model and compared the numerical solutions with different other numerical methods and exact solution as follow.

Example 1: Consider the Bratu-type initial value problem

$$\begin{cases} y'' - 2e^{y} = 0, \ 0 < x < 1 \\ y(0) = 0, \quad y'(0) = 0 \end{cases} \tag{46}$$

whose exact solution is $y(x) = -2\ln(\cos(x))$

Table 1. The comparison of absolute errors for Example 1 at different values of the mesh size h with different numerical methods

	Absolute errors at $h = 0.1$			
x	Method in[7]	Method in[8]	Method in [10]	Present Method
0.1	6.7100e-6	4.3876e-13	6.4102e-7	2.8436e-9
0.2	9.5500e-6	4.5402e-10	9.7469e-6	1.2788e-7
0.3	3.3100e-6	2.6638e-8	4.5299e-5	3.9593e-7
0.4	8.0400e-6	4.8488e-7	1.2711e-4	3.4141e-6
0.5	8.4800e-6	4.6664e-6	2.6867e-4	4.4904e-6
0.6	2.0300e-5	3.0124e-5	4.8365e-4	6.8988e-6
0.7	7.1500e-5	1.4821e-4	8.3679e-4	1.1741e-5
0.8	2.9100e-4	6.0039e-4	1.6005e-3	2.1580e-5
0.9	1.0500e-3	2.1074e-3	3.6497e-3	4.2756e-5
1.0	3.5300e-3	6.6498e-3	9.3915e-3	9.2517e-5

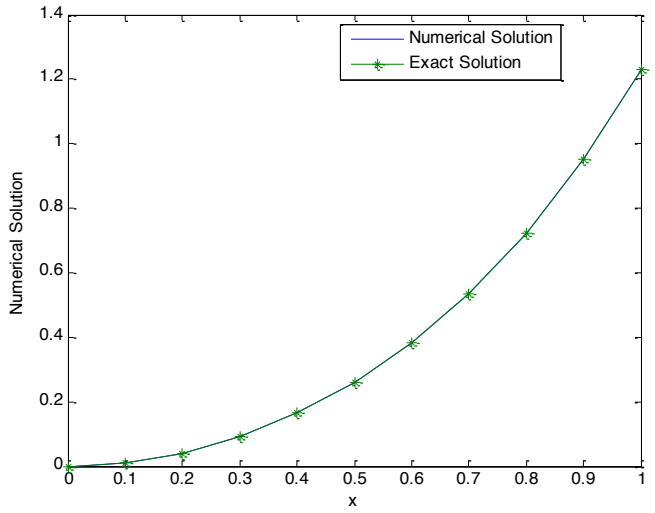

Fig. 1. Plot of exact and approximated solution of Bratu-type equation using predictor-corrector method for Example 1 with mesh length $h = 0.1$.

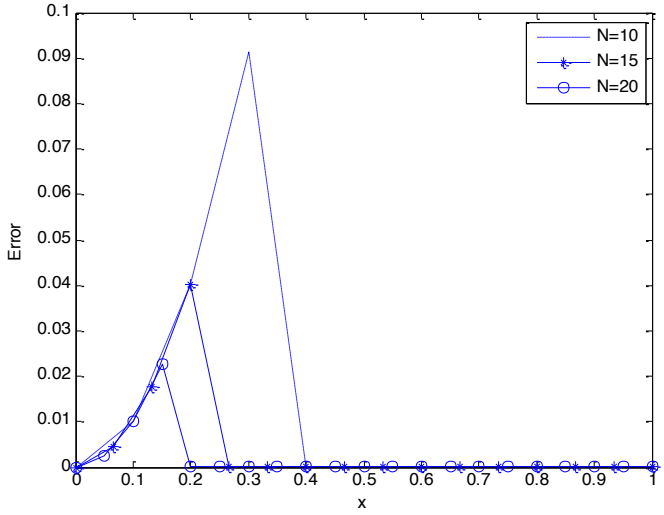

Fig. 2. Point-wise absolute error of Example 1 for different values of number of meshes points.

Example 2: Consider the Bratu-type initial value problem

$$\begin{cases} \dfrac{d^2y}{dx^2} = -\pi^2 e^{-y}, \\ y(0) = 0, \quad y'(0) = \pi \end{cases} \tag{47}$$

whose exact solution is $y(x) = \ln(1 + \sin(\pi x))$

Table 2. The comparison of absolute errors for Example 2 at different values of the mesh size h

x	Absolute errors at $h = 0.1$		
	Exact value	Method in [9]	Present Method
0.1	0.26928	3.20777e-4	3.4129e-5
0.2	0.46234	2.37600e-5	5.7752e-5
0.3	0.59278	3.58700e-5	7.9099e-5
0.4	0.66837	8.01000e-5	2.7368e-4
0.5	0.69315	1.19500e-4	4.2841e-5
0.6	0.66837	1.66200e-4	6.8607e-5
0.7	0.59278	2.20200e-4	1.3754e-4
0.8	0.46234	2.85100e-4	1.8845e-4
0.9	0.26928	4.03400e-4	2.2350e-4
1.0	2.2204e-16	5.37400e-4	2.1737e-4

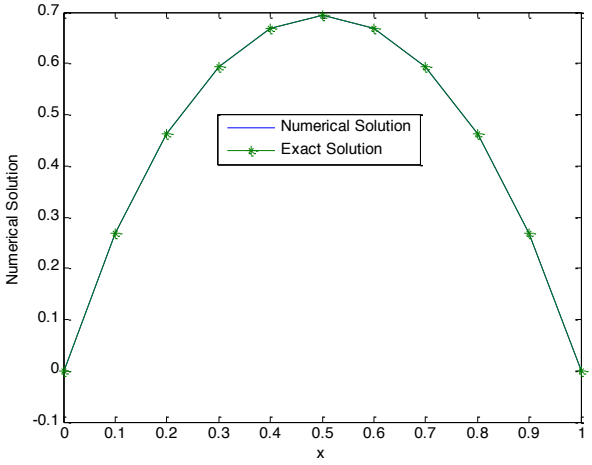

Fig. 3. Plot of exact and approximated solution of Bratu-type equation using predictor-corrector method for Example 2 with mesh size $h = 0.1$.

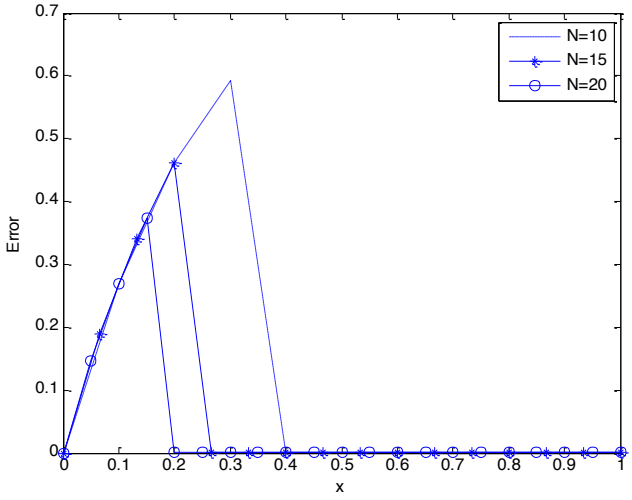

Fig. 4. Point-wise absolute errors of Example 2 for different values of number of mesh points.

5. Discussion and Conclusion

This study introduces numerical solutions of second order initial value problems of Bratu-type equations using predictor-corrector method. The stability and convergence of the scheme are investigated and established well. The numerical solutions are tabulated in terms of point wise absolute errors and observed that the present method improves the findings of some existing numerical methods reported in the literature (Table 1 and 2). Moreover, behaviors of the numerical solution (Figure 1 and 3) and point-wise absolute errors (Figure 2 and 4) were shown in figures. According to the plotted figures one can clearly observe that the numerical and exact solutions agree very well and as number of mesh point increases or as step size decreases, the point-wise absolute error decreases which clearly indicates the convergence of the present scheme. Concisely, the present method gives more accurate solution for solving second order initial value problems of Bratu-type equations.

References

[1] King A.C. Billingham J. and Otto S.R., Differential Equations: Linear, Nonlinear, Ordinary, Partial. Cambridge University Press, New York, (2003).

[2] Jain M.K., Iyengar S.R.K. and Jain R.K., Numerical Methods for Scientific and Engineering Computation, Sixth Edition, New Age International Publishers, (Formerly Wiley Eastern Limited), New Delhi.,2007.

[3] Abdelmajid El hajaji, Khalid Hilal, El merzguioui Mhamed and Elghordaf Jalila, A Cubic Spline Collocation Method for Solving Bratu's Problem, IISTE J. Mathematical Theory and Modeling, 3(14), 2013.

[4] Batiha B.,Numerical Solution of Bratu-Type Equations by the Variational Iteration Method, Hacettepe J. Math. Stat., 39(1), 23-29, 2010.

[5] Aksoy Y, Pakdemirli M., New perturbation–iteration solutions for Bratu-type equations. Computers & Mathematics with Applications, 59(8), 2802-2808, 2010.

[6] Duan JS, Rach R, Baleanu D, Wazwaz AM., A review of the Adomian decomposition method and its applications to fractional differential equations, Communications in Fractional Calculus.3(2),73-99, 2012.

[7] Moradi E, Babolian E, Javadi S., The explicit formulas for reproducing kernel of some Hilbert spaces, Miskolc Mathematical Notes, 16(2), 1041-1053, 2015.

[8] Darwish MA, Kashkari BS., Numerical solutions of second order initial value problems of Bratu-type via optimal homotopy asymptotic method, American Journal of Computational Mathematics, 4(2):47, 2014.

[9] Habtamu, G.D, Habtamu, B.Y., Solomon B.k., Numerical solutions of second order initial value problems of bratu-type equation using higher ordered Rungu-kutta method, International Journal of Scientific and Research Publications, 7(10), 187–197, 2017.

[10] Butcher, J. C., Numerical Methods for Ordinary Differential Equations, John Wiley and sons Ltd., New Zealand, 2008.

International Journal of Engineering & Applied Sciences (IJEAS)
Vol. 12, Issue 1 (2020) 32-42
http://dx.doi.org/10.24107/ijeas.717059
Int J Eng Appl Sci 12(1) (2020) 32-42

Analysis of the Effects of Different Frequency Values on the Loss of Transformers

Yıldırım Özüpak [a*], *Mehmet Salih Mamiş* [b]

[a] *Dicle University, Silvan Vocational School, Diyarbakır, Turkey*
[b] *İnönü University, Engineering Faculty, Electrical&Electronic Engineering, Malatya, Turkey*
[*] *E-mail address*: yildirim.ozupak@dicle.edu.tr [a], mehmet.mamis@inonu.edu.tr [b]

ORCID numbers of authors:
0000-0001-8461-8702[a], *0000-0002-6562-0800*[b]

Received date: 09.04.2020
Accepted date: 23.04.2020

Abstract

Accurate simulation and loss estimation in power transformers are crucial for both the design phase and useful life of the transformer. In this study, core losses and magnetic flux densities of a power transformer for different frequency values are calculated. For this, ANSYS @ MAXWELL software based on the Finite Elements Method (FEM) and the 3D simulation model of the transformer were examined. The results obtained from simulations performed at 50 Hz and 60 Hz frequencies were compared with theoretical and experimental results. It has been observed that increasing the frequency causes increased heat and loss in the core of the transformer.

Keywords: Core loss, power transformer, magnetic flux density, frequency.

1. Introduction

Modeling and correct simulation of power transformers has always been a challenge for engineers. Power transformers are one of the most expensive elements of the energy system. Therefore, the prediction that the transformer is working correctly and possible malfunctions have always been a problem for engineers. High frequency models of power transformers are recommended for analysis of transient interaction between transformers and power system [1]. An algorithm and transformer model is proposed to identify different internal faults that cause power interruption in the transformer [2]. In recent years, the Finite Element Method (FEM) has been widely used to model various nonlinear materials and permanent magnetization of these materials [3-5]. In cases where partial discharge occurs in transformer winding FEM is used to calculate transformer parameters [6]. In recent years, various powerful software have been developed to calculate transformer parameters, operating modes and different types of loss [7]. In this paper, the 3D power transformer model given in Fig. 1 is presented below to calculate the core losses and magnetic flux density in the transformer section. Since the core losses are calculated in case of transformer operation at 50 Hz frequency without load, only the low voltage winding is energized with nominal voltage.

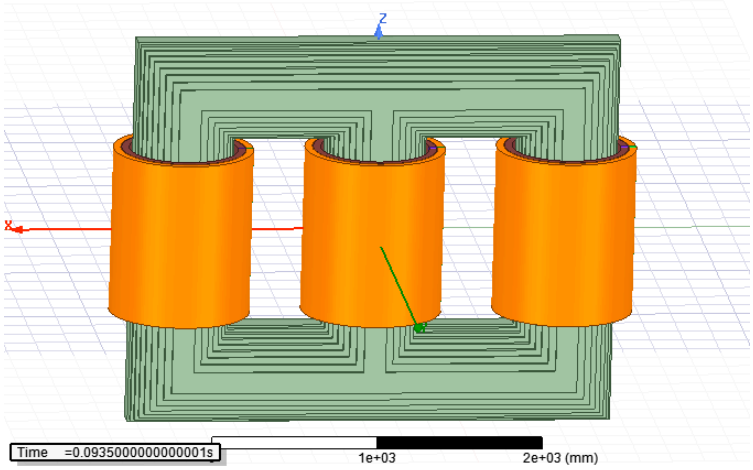

Fig. 1. 3D model of the transformer

The distribution of the magnetic flux density in the core section is shown by simulation. Flux density is calculated at different time intervals. Flux density information helps to identify parts of the nucleus near the saturation point. Depending on the flux density information, the saturation characteristic of the nucleus and the core losses are determined depending on the characteristic and the transformer design can be modified to optimize them.

2. Modeling of Transformer and Electromagnetic Accounts

Based on the actual transformer dimensions and geometry, FEM models are created for 3D simulations of low frequency temporary electromagnetic fields. The basic process of transient simulation includes regional and temporal separation of physical equations. There are various approaches for regional separation, such as finite differences, finite elements and limited volumes. Finite Element Method (FEM) is the most widely used method in engineering applications. With this method, complex, non-homogeneous and anisotropic materials can be modeled and complex geometries can be analyzed using irregular meshes (mesh) [8-9].

FEM solves Maxwell's equations based on a given excitation and frequency value. Simulation is accomplished by field parsing along the time axis to simultaneously solve all time stages. In the designed transformer model, boundary conditions, outer geometry and the properties of all materials are defined on the design in the program environment. The magnetic core is characterized by the B-H curve of magnetization and fine laminations. These characteristic features are used in the simulation of the transformer model. The characteristic B-H curve of the material used in the core is given below in Fig. 2. The P-B curve, which is the specific core losses given in Fig. 3 below, is also introduced in the simulation environment and the core losses are calculated for the frequencies of 50 Hz and 60 Hz.

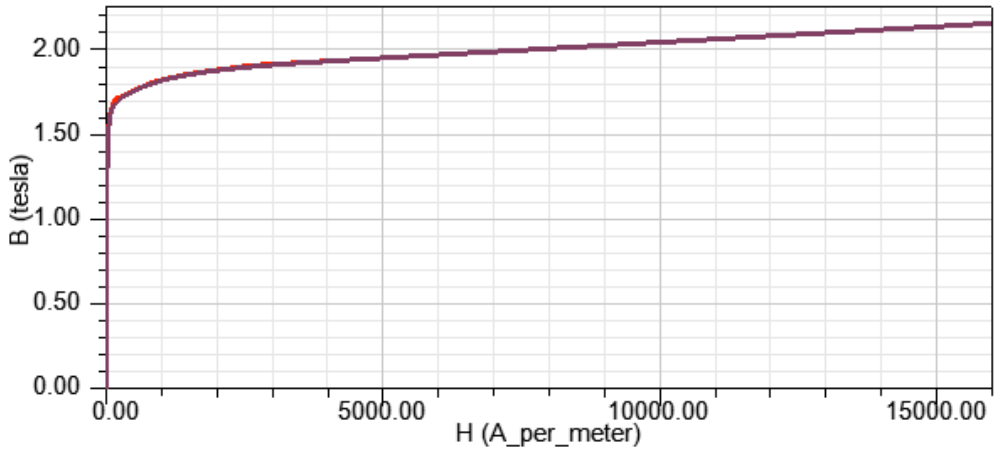

Fig. 2. B-H curve of core laminations

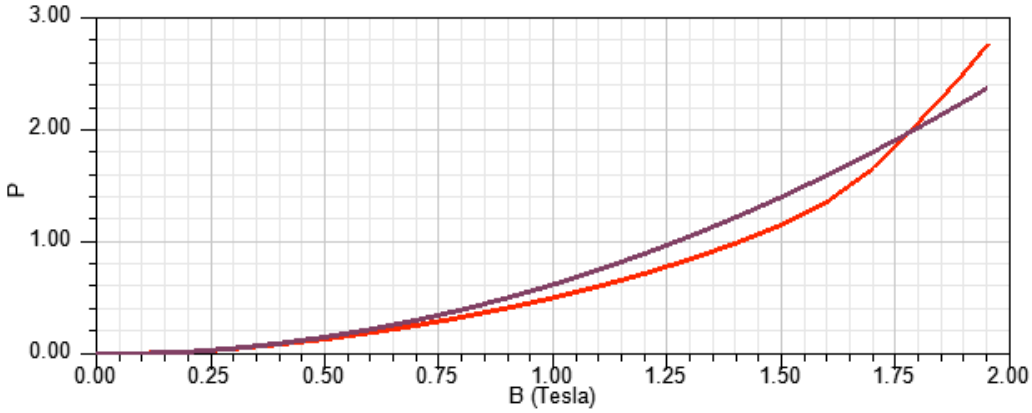

Fig. 3. P-B curve of core losses

Where; B is the magnetic flux, H is the magnetic flux intensity and P is the losses per kg. Also, the red curve is the actual curve. The black curve is the regression of the original curve.

The properties and parameters of the transformer designed in ANSYS@MAXWELL environment are given in Table 1 below.

Table 1. Design features of the transformer

Rated Power	15 MVA
HV	33.000 V
LV	11.000 V
Core loss	12.500 W
Copper loss	97.000 W
HV Winding Resistance	1.7 Ω
LV Winding Resistance	40 mΩ
$\%U_k$	%11
Io	% 0.44
HV connection	Delta

LV connection	Star
HV turn number	135
LV turn number	665
HV phase current	784 A
LV phase current	156 A
Current density	1.8 A/m^2

In general, core loss (Pc) is divided into two components: hysteresis losses (Ph) and eddy current losses (Pe). According to the Steinmetz equation, the measurement and calculation of core losses are done with the normally varying Mag-B and frequency of sinusoidal flux of the frequency. These measurements and calculations are often modeled with a bi-term function of the form depending on the standard coil.

$$P_c = P_h + P_e = k_h f B^n + k_c f^2 B^2 \quad (1)$$

Where, kh, kc and n are coefficients that depend on lamination, material thickness, conductivity and other factors [10].

In this study, the calculation of core losses are made according to:

$$P_c = P_h + P_e + P_{excess} = K_1 B_m^2 + K_2 B_m^{1.5} \quad (2)$$

Eddy current loss:

$$P_e = k_c (f B_m)^2 \quad (3)$$

Hysteresis loss:

$$P_h = k_h f {B_m}^2 \quad (4)$$

Excessive loss:

$$P_{exces} = k_e (f B_m)^{1.5} \quad (5)$$

For that reason:

$$K_1 = k_h + k_c f^2 \quad (6)$$

$$K_2 = k_e f^{1.5} \quad (7)$$

The k_1 and k_2 coefficients are obtained by minimizing the function. Eddy current loss coefficient is calculated as follows:

$$k_c = \pi^2 \sigma \frac{d^2}{6} \quad (8)$$

Where; σ conductivity and d is the thickness of the lamination layer.

In this case, core losses in transformer models are defined as total losses for a specific frequency such as 50 Hz or 60 Hz (P-B curve). When the design of the transformer model is started with the starting frequency of 60 Hz and the model frequency is changed to 50 Hz, both the amplitude of the input phase voltage and the factor of the transformer are reduced. This prevents the transformer from overheating when the operating frequency of the transformer is changed from 60 Hz to 50 Hz. Because when the frequency is changed, the currents passing through the windings do not change. Power losses are calculated at both operating frequencies. For core losses, only one energetic winding should be considered. An exponentially increased voltage source is applied to eliminate sudden currents and shorten the simulation time as given in Fig. 4 below.

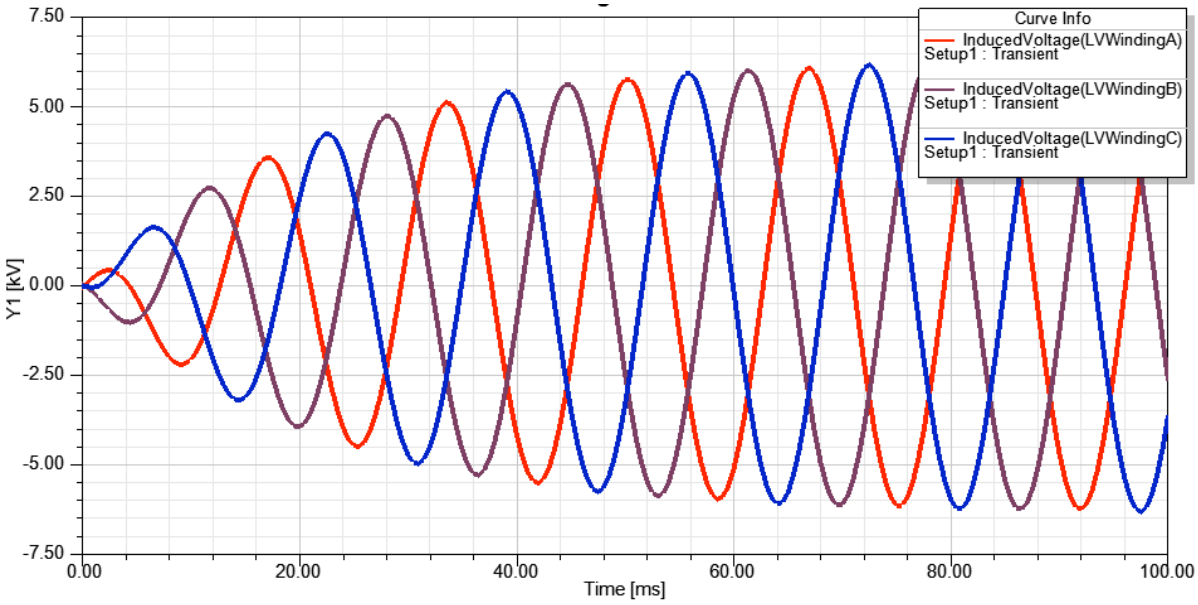

Fig. 4. Input voltage at 50 Hz

In order to calculate the magnetic flux density B, the magnetic vector potential A must be present. For this purpose, all model geometry is divided into many elements, usually triangles, where A is approximately matched by a simple function. Mesh (mesh) formed by finite elements in 3D model is presented in Fig. 5.

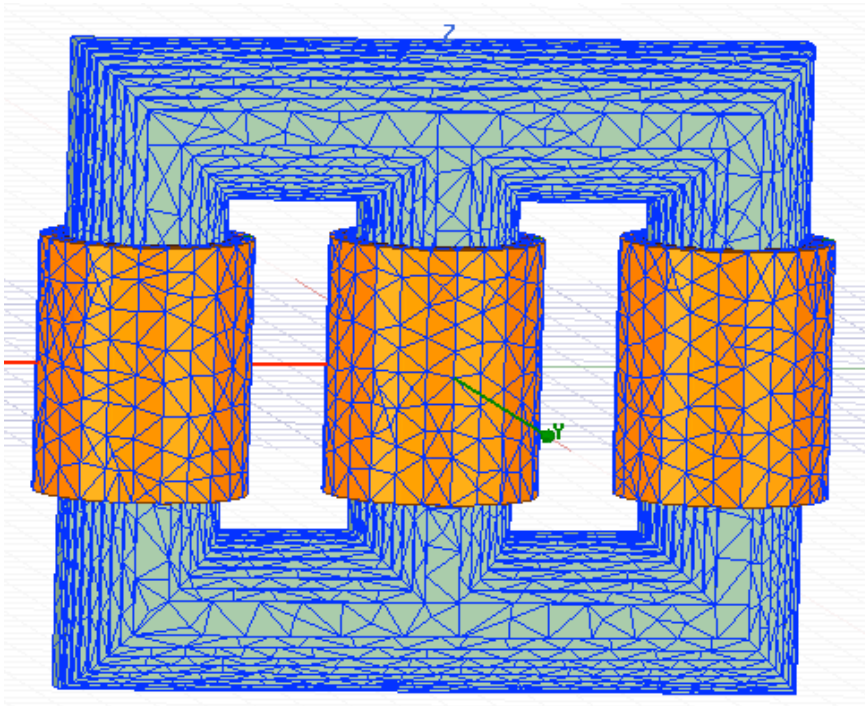

Fig. 5. Mesh in transformer models.

3. Simulation and Analysis of the Model

In transient simulation, analysis is performed for predefined time interval and time step. From the simulation of the 3D model of the designed transformer, core losses were obtained for two different frequencies of 50 Hz and 60 Hz. Core losses are calculated by taking the average of the total losses obtained over the given time interval over time.

3.1. Analysis of Losses

From the simulation of the 3D model, core losses and magnetic flux distribution were obtained for two different frequencies of 50 Hz and 60 Hz. Graphs of core losses, eddy current losses and hysteresis losses depending on all the above variables are presented in the Figs below.

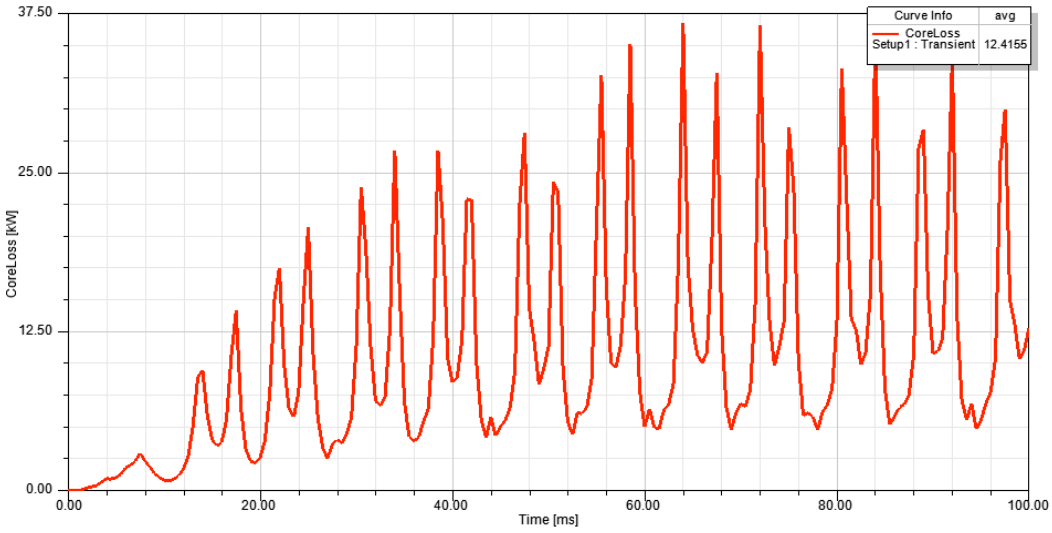

Fig. 6. Core loss of the model at a frequency of 50

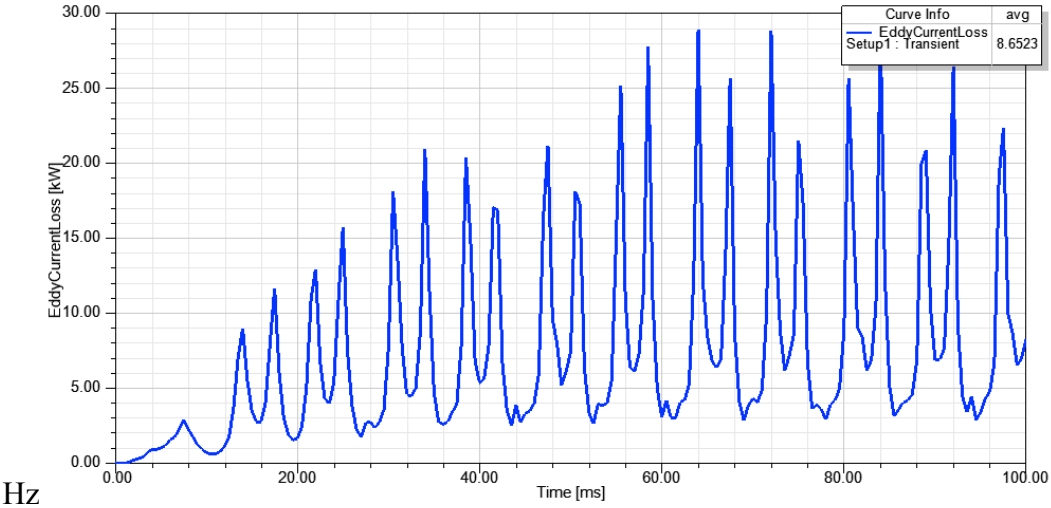

Hz

Fig. 7. Eddy loss of the model at a frequency of 50 Hz

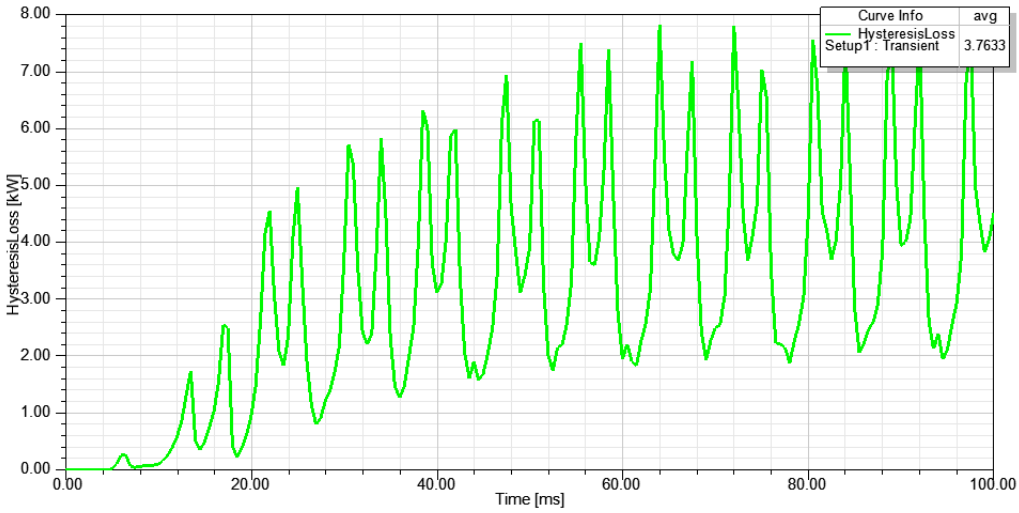

Fig. 8. Hysteresis loss of the model at 50 Hz frequency

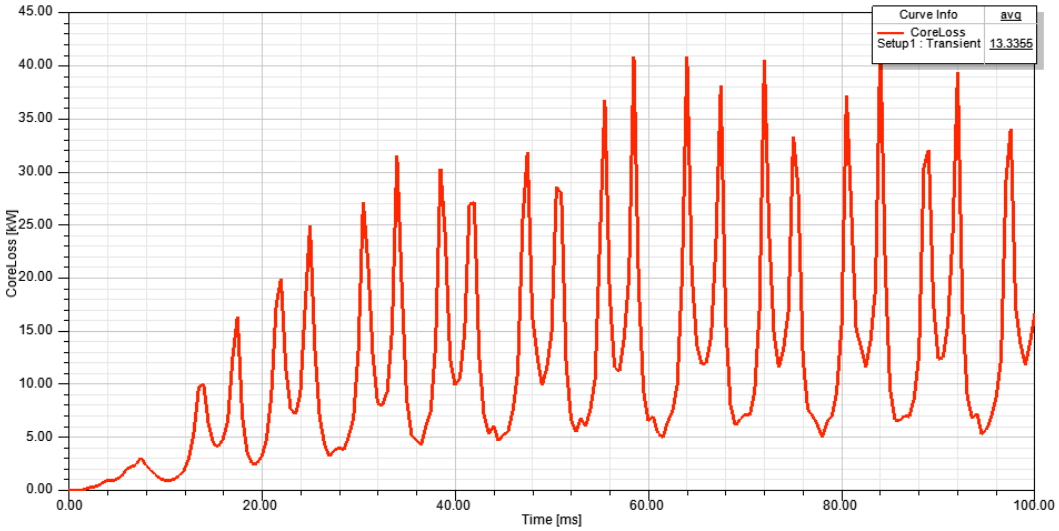

Fig. 9. Core loss of the model at a frequency of 60 Hz

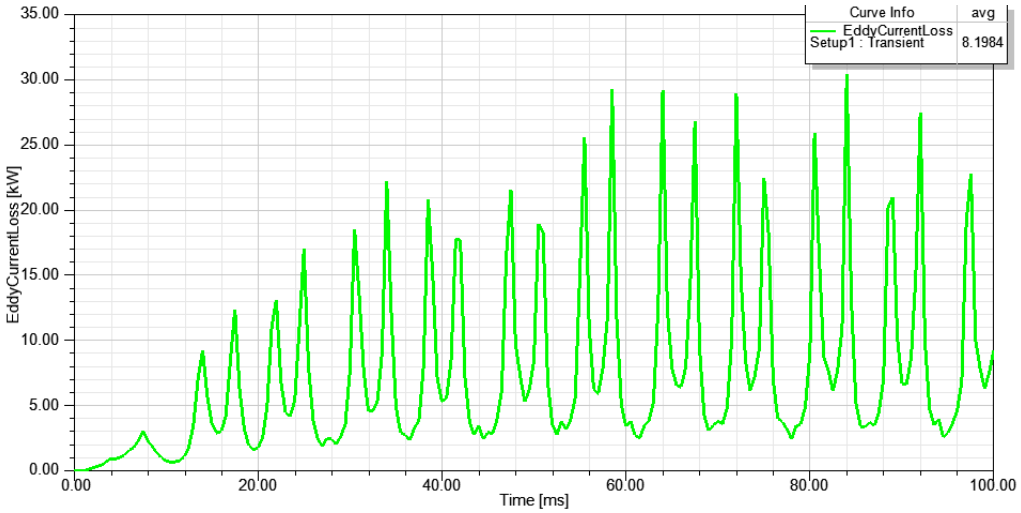

Fig. 10. Eddy loss of the model at a frequency of 60 Hz

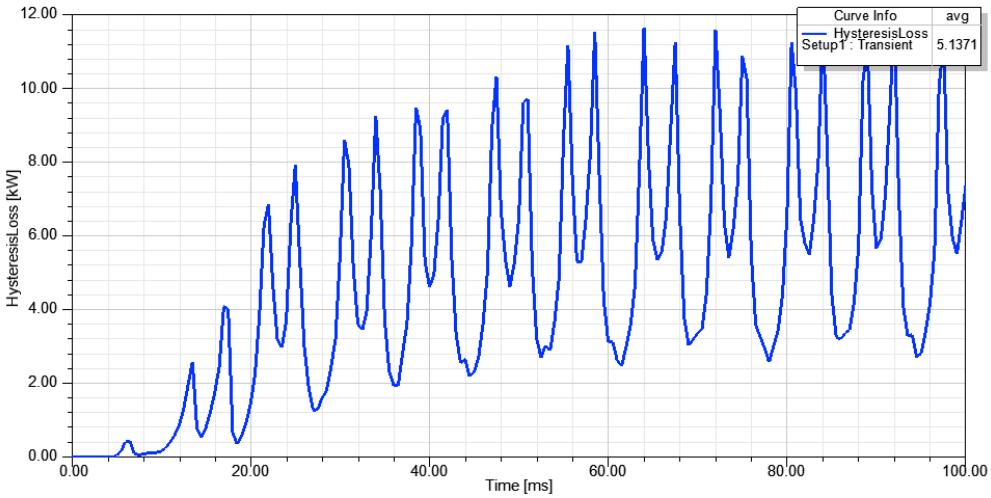

Fig. 11. Hysteresis loss of the model at a frequency of 60 Hz

The loss values of the transformer at different frequencies are compared in Table 2 below.

Table 2. Loss values at different frequencies.

	Simulation results		*Theoretical results*
	50 Hz	60 Hz	50 Hz
Core loss (kW)	12.41	13.34	12.36
Eddy current loss (kW)	8.65	8.2	8.59
Hysteresiz loss (kW)	3.76	5.14	3.77

There is a difference between 50 Hz and 60 Hz core and copper loss values of the transformer. The core losses tested at 50 Hz are 12.5 kW. The designed model is simulated within both the frequencies of 50 Hz and 60 Hz. As expected, core losses were lower at a frequency of 50 Hz.

3.2. Electromagnetic Field Analysis

The operation of the core of the transformer close to the saturation point increases losses and heat dissipation, reduces efficiency. Therefore, the flux density was analyzed at different time intervals for both frequencies. The 3D magnetic flux density of the transformer is presented Fig. 12 below.

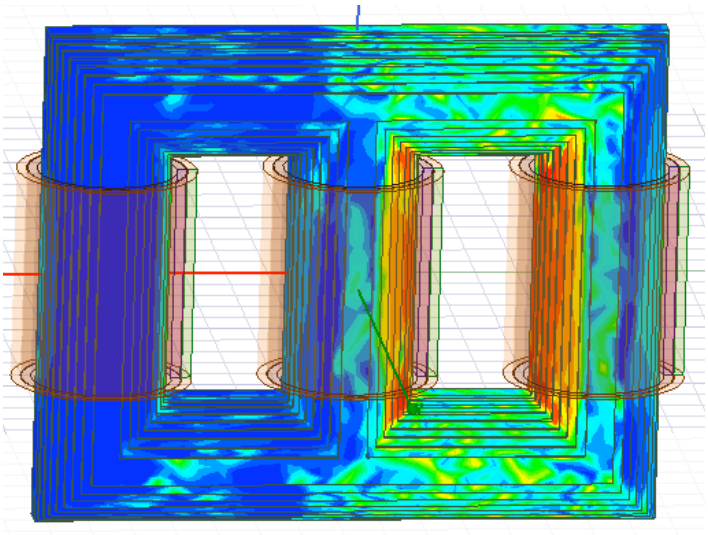

Fig. 12. Flux density distribution in 3D transformer model for 50 Hz frequency.

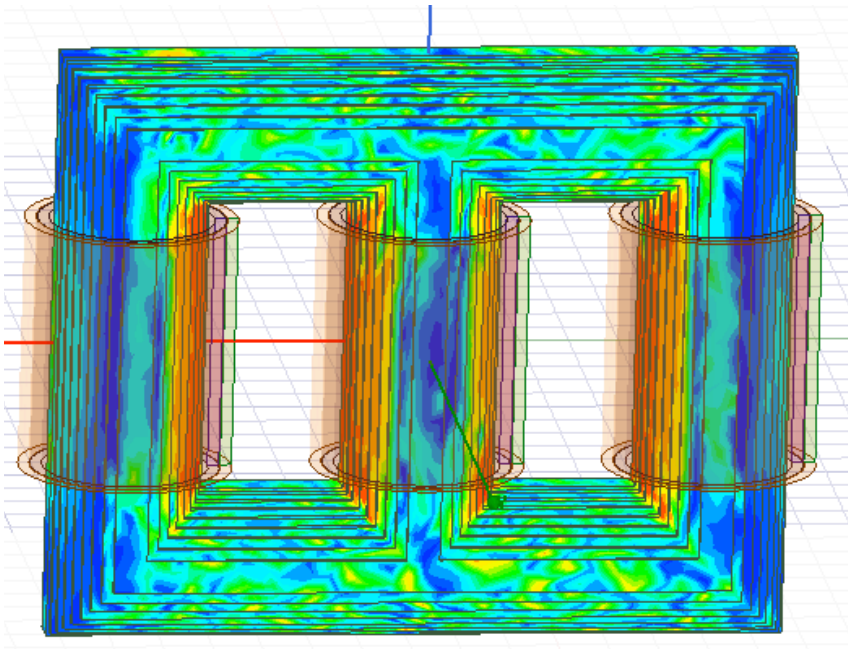

Fig. 13. Flux density distribution in 3D transformer model for 60 Hz frequency

It is clear that the flux density distribution in the core cross section of the transformer, which operates at 50 Hz and 60 Hz frequency without load, determines the saturation point well. As expected, the density of flux was higher than the frequency of 50 Hz at 60 Hz, since the loss of core occurred more in the model working at 60 Hz.

When the results in Table 2 are compared, it shows that there is a difference between the core loss values obtained in the 3D models of the transformer. The core losses tested at 50 Hz are 12.5 kW. 3D models are simulated within both the frequencies of 50 Hz and 60 Hz. As expected, core losses are low at a frequency of 50 Hz. All physical core loss effects are not calculated with the FEM model. Unpredictable effects include variations such as mechanical pressure on laminations, edge roughness loss, gradual hollow flux, circulation current and sheet loss.

For accurate estimation of flux density in different parts of the transformer, it is important to correctly estimate the parts of the transformer, called the weak part, where the core material is close to the saturation point (B-H). Operation of the transformer close to the core saturation point increases losses and heat dissipation, decreases efficiency. Therefore, the flux density is analyzed at different time intervals for both frequencies.

4. Conclusions

Knowing the losses in electrical devices is important in terms of both design and use of the device. Therefore, estimating losses with the right simulation models helps designers design highly energy efficient devices. FEM based transformer simulation model is presented. The obtained 3D models provide the calculation of the main losses for the three-phase symmetrical power supply. Models are powered by 50Hz and 60Hz frequency power supplies. Losses occurring at 50 Hz are lower than losses occurring at 60 Hz due to low frequency losses. The flux density distribution in the transformer section was also calculated.

From the results obtained from all models, it has proven that the transformer which operates without a load works well above the saturation point of the core.

References

[1] E.I. Amoiralis, M.A. Tsili, A.G. Kladas, Transformer Design and Optimization: A Literature Survey, IEEE Transactions on Power Delivery, 24(4), 1999-2024, 2009
[2] P. S. Georgilakis, M. A. Tsili, and A. T. Souflaris, A heuristic solution to the transformer manufacturing cost optimization problem, J. Mat. Process. Technol., 181, 260–266, 2007.
[3] Yugendrao K. N., Structural Modeling of a Three Phase Core type Transformer using ANSYS Maxwell 3D, Internatıonal Journal Of Innovatıve Research In Electrıcal, Electronıcs, Instrumentatıon And Control Engıneerıng, 4(4), 17-20, 2016.
[4] S. Vasilija, FEM 2D and 3D design of transformer for core losses computation, Scıentıfic Proceedings XIV Internatıonal Congress, Machınes. Technologıes. Materıals., 2017– Summer Sessıon Volume V, 345-348.
[5] M.B.B. Sharifian, R. Esmaeilzadeh, M. Farrokhifar, J. Faiz, M. Ghadimiand G. Ahrabian, computation of a single-phase shell-type transformer windings forces caused by ınrush and short-circuit currents, Journal of Computer Science, 4(1), 51-58, 2008.
[6] T. Orosz, G. Kleizer, T. Iváncsy, Z. Á. Tamus, Comparison of methodsforcalculation of core-form power transformer'score temperature rise, Periodica Poly technica Electrical Engineering and Computer Science, 60(2), 88-95, 2016.
[7] M. L. Myint, Y. A. OO, Analysis of distribution transformer design using FEA, International Journal of Scientific Research Engineering &Technology (IJSRET), 3(4), 773-775, 2014.
[8] N. A. M. Yusoff, K. A. Karim, S. A. Ghani, T. Sutikno, A. Jidin, Multiphase transformer modeling using finite element method, International Journal of Power Electronics and Drive System (IJPEDS), 6(1), 56-64, 2015.
[9] Y. Chen, P.Pillay, An Improved Formula for Lamination Core Loss Calculation in Machine Operating with High Frequency and High Flux Density Excitation, IEEE, 2002
[10] User's guide – Maxwell 2D/3D. 2019

International Journal of Engineering & Applied Sciences (IJEAS)
Vol. 12, Issue 1 (2020) 43-56
http://dx.doi.org/10.24107/ijeas.727320
Int J Eng Appl Sci 12(1) (2020) 43-56

Buckling Analysis of Functionally Graded Plates Using Finite Element Analysis

Nihat CAN [a], Naci KURGAN [b], Ahmed HASSAN [c]*

[a,b,c] Department of Mechanical Engineering, Ondokuz Mayıs University,55139, Samsun, Turkey
[*]E-mail address: 13210381@stu.omu.edu.tr [a], naci.kurgan@omu.edu.tr [b], 15210457@stu.omu.edu.tr [c]

ORCID numbers of authors:
0000-0002-5741-0890[a], 0000-0001-7297-7249[b],
0000-0002-4880-0184[c]

Received date: 26.04.2020
Accepted date: 20.05.2020

Abstract

The present study aims to give critical buckling loads of rectangular functionally graded (FG) plates for various types of boundary conditions. The finite element formulation of stability of plates is introduced and the procedure is applied to obtain critical buckling loads of a plate for two types of boundary conditions: (a) CFFC: two parallel edges are clamped and free along the other two; (b) FFFC: the plate is clamped along one edge and free along all the others. Variation of mechanical properties of the FG plate along the length and the variation along the thickness have been both considered. According to the function of elasticity modulus variation, results have been obtained for various power indices of the varying function. Results compare well with those obtained using shell elements in ANSYS.

Keywords: FGM, buckling of plates, finite element method, ANSYS.

1. Introduction

Typical composite structures with a mixture of two or more different material phases can be referred to as functionally graded plates (FG plates) and the performance of the plates is achieved by adjusting the component formula that forms the structure. Such plates completely inherit the properties of their components and have some special properties such as high hardness, high fatigue resistance, wear resistance. For example, ceramic and metal mixed FG plates have thermal properties of ceramics while also having ductility of metals. Therefore, FG plates, aircraft, vehicles, ships and so on. It is widely used in engineering applications including. Generally, FG plates are subjected to different types of mechanical loads depending on the environment in which they operate and are located. In particular, the behavior of the structure under mechanical loads causing static bending and buckling is very important for the design of the structure. Therefore, it is important to examine the static bending and buckling behavior of FG plates.

Levy [1] proposed a method to demonstrate the buckling behavior of rectangular plates subjected to lateral pressure and edge compression. Javaheri and Eslami [2] investigated the buckling analysis of functionally graded plates under in-plane compression loads based on classical plate theory. Chen and Liew [3] presented buckling analysis using a net method to determine the critical buckling loads of functionally graded rectangular plates exposed to nonlinear loads at plane edge loads. Vel and Batrab [4] developed a three-dimensional precise solution for simply supported free and forced vibrations of functionally graded rectangular plates. Chi and Yen [5], a functionally classified rectangular material plate with simple constrained conditions subjected to transverse loading. Shariah and Eslami [6] obtained a closed-form solution to the buckling of the FG plate, based on the theory that the plate was loaded with mechanical, thermal loads and bending loads for third order shear deformation. Modeling and analysis of functionally classified material plates was performed by Birman and Larry [7]. An analysis of the classical plate theory and the expansion of the Fourier series was achieved by Using the second-order shear deformation theory, the natural frequency of the functional-grade rectangular plate was estimated by Shahrjerdi et al. [8]. Theoretical analysis of FGM plates based on the physical boundary surface was discussed by Zhangand Zhou [9]. Prakashetal [10] examined the effect of neutral surface position on the nonlinear stability behavior of functionally graded plates using the finite element method. Mohammadi et al. [11] have analytically solved the buckling analysis of simply supported, moderately thick, functionally graded rectangular plates with two opposite sides. Talha and Singh [12] researched the static and free vibration analysis of functionally classified material plates by using finite element model and high-grade shear deformation theory. Pendhari et al. [13] established analytical and mixed semi-analytical static solutions for a simple supported plate that is functionally rated in a rectangular form. Singha et al. [14] utilized the finite element method in the analysis of nonlinear behavior of functionally graded plates under transverse load based on the first order shear deformation theory. Hashemi et al. [15] done the new fully closed form method for free vibration analysis of functionally graded rectangular thick plates, based on Reddy's theory of the third-order shear deformation plate. Bousahla et al. [16] offered a plate theory for the buckling analysis of functionally graded plates subjected to uniform, linear and nonlinear temperature increases throughout the thickness. Demirhan and Taskin [17] submitted Levy's solution, which is based on four variable plate theory, for bending analysis of functionally graded sandwich plates. By Mohseni et al. [18], higher grade shear and normal deformable plate theory was employed for analytical solution of static analysis of functionally graded thick micro-plates. Although there have been many studies on the analysis of isotropic and laminated composite beams (i.e., [19-22]), however, the research effort dedicated to stability analysis of rectangular of FG plates has been very limited.

In this study, stability analysis of rectangular FG plates was carried out using thin plate theory under various boundary conditions. The ceramic-metal (Alumina-Aluminum) composition of the FGM was chosen for numerical results. Using the finite element method, critical buckling loads for two types of boundary conditions were found. These boundary conditions are as follows: 1- The plate is held along the edges to which the load is applied and free at the other edges. 2- The plate was applied to be held along one edge and free along the other three edges. The change in the characteristics of the FG plate was considered in two ways. The model was formed by assuming that the elastic properties of the plate changed along the length of the plate, and that the elastic properties of the plate changed along the thickness of the plate.

2. FGM Structures

In order to analyze FGM structures as shown in Fig. 1, two types of FG variation have been considered. In the first, the elasticity modulus varies according to the function given in the equation $E(x) = (E_1 - E_2)(\frac{x+L}{2L})^n + E_2$. The other variation function is given as $E(x)=E_1e^{-\lambda x}$.

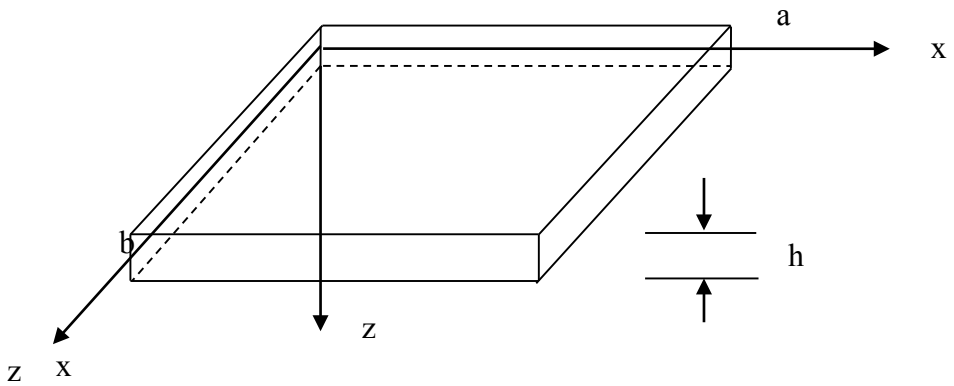

Fig. 1. A Rectangular Plate and Coordinate System

3. Provision of Solution Method

The efficiency and reality of numerical methods is first checked with the analytical results obtained for the square plate homogeneous. In the equations given in $E(x) = (E_1 - E_2)(\frac{x+L}{2L})^n + E_2$ and $E(x)=E_1e^{-\lambda x}$, the cases are related to a functionally graded plate with λ and n factors. If these are chosen to be zero, the plate will be homogenous. Also, when the inclination angle is zero with the λ=0 and n=0 the plate is a square homogenous plate which has the analytical solution given in the literature [23] as $N_x = 10.07\frac{\pi^2 D}{a^2}$; where D is the plate stiffness. To compare the results obtained from FEM and ANSYS a plate with varying thicknesses is used. For a plate with the dimensions a=0.5, h from 0.0005 to 0.005 and E= 380.E+09 GPa. The subscripted terms in Table 1 that is $()_b$ (plate base) and $()_t$ (plate tip) are the material properties of FG rectangular plate. Table 2. shows results from analytical method and finite element method to observe the difference. Note the results are close to each other for the homogenous case.

Table 1. Material properties of the FGM plate.

Properties	Unit	Aluminum; $()_b$	Alumina; $()_t$
E	Pa	70×10^9	380×10^9
υ	---	0,3	0,3

Table 2. Critical buckling loads obtained analytically and by FEM, ANSYS for the homogenous square plate.

h	Critical Buckling Load (N_x) (FEM)	Critical Buckling Load (N_x) (ANALYTICALL)	Critical Buckling Load (N_x) (ANSYS)
0.0005	1734.4789	1729.264	1733.4698
0.001	13875.8309	13834.1123	13874.8219
0.0015	46830.9239	46690.1235	46829.8392
0.002	111006.6472	110672.8982	111005.7647
0.0025	216809.8125	216157.959	216808.7185
0.003	374647.3908	373520.9879	374646.4009
0.0035	594926.2204	593137.5341	594927.4202
0.004	888053.178	885383.1855	888052.872
0.0045	1264434.748	1260633.139	1264433.848
0.005	1734478.5	1729263.672	1734477.6

4. Formulation with FEM and Solution Procedure

Equation of total tensile energy of a rectangular plate:

$$U = \frac{D_{FGM}}{2}\int_{-a}^{a}\int_{-b}^{b}\left\{\left(\frac{\partial_2 w}{\partial x_2}+\frac{\partial^2 w}{\partial y^2}\right)^2 - 2(1-\nu)\left[\left(\frac{\partial^2 w}{\partial x \partial y}\right)^2 - \frac{\partial^2 w}{\partial x^2}\frac{\partial^2 w}{\partial y^2}\right]\right\}dxdy$$
$$-\frac{1}{2}\int_{-a}^{a}\int_{-b}^{b}\left\{N_x\left(\frac{\partial w}{\partial x}\right)^2 + 2N_{xy}\frac{\partial w}{\partial x}\frac{\partial w}{\partial y} + N_y\left(\frac{\partial w}{\partial y}\right)^2\right\}dxdy \quad (1)$$

where the stiffness matrix of FGM plate [D_{FGM}] is

$$[D]_{FGM} = \frac{\mathrm{E}(x)h^3}{12(1-\nu^2)}\begin{bmatrix} 1 & \nu & 0 \\ \nu & 1 & 0 \\ 0 & 0 & \frac{1-\nu}{2} \end{bmatrix} \quad (2)$$

The Elasticity Module, which changes along the X axis, is defined as displacements in a plate: w= off-plane deviation, $\theta_x = \frac{\partial w}{\partial y}$; slope of the plate in the y direction, $\theta_y = \frac{\partial w}{\partial x}$; slope of the plate in the x direction, $\theta_{xy} = \frac{\partial^2 w}{\partial x \partial y}$;

Deformation equivalents are in matrix form:

$$\{\varepsilon\} = \begin{Bmatrix} -\dfrac{\partial^2 w}{\partial x^2} \\ -\dfrac{\partial^2 w}{\partial y^2} \\ -2-\dfrac{\partial^2 w}{\partial x \partial y} \end{Bmatrix} \tag{3}$$

and the stresses are:

$$\{\sigma\} = \begin{Bmatrix} M_x \\ M_y \\ M_{xy} \end{Bmatrix} \tag{4}$$

where

$$M_x = \frac{E(x)h^3}{12(1-\nu^2)}\left(-\frac{\partial^2 w}{\partial x^2} - \nu\frac{\partial^2 w}{\partial y^2}\right) \qquad M_y = \frac{E(x)h^3}{12(1-\nu^2)}\left(-\frac{\partial^2 w}{\partial y^2} - \nu\frac{\partial^2 w}{\partial x^2}\right)$$

$$M_{xy} = (1-\nu)\frac{E(x)h^3}{12(1-\nu^2)}\left(-\frac{\partial^2 w}{\partial x \partial y}\right) \tag{5}$$

since modulus of elasticity varies along the x-axis.
Therefore, stresses are in matrix form:

$$\{\sigma\} = \begin{Bmatrix} M_x \\ M_y \\ M_{xy} \end{Bmatrix} = [\mathrm{D}]_{FGM}\ \{\varepsilon\} = [\mathrm{D}]_{\mathrm{FGM}} \begin{Bmatrix} -\dfrac{\partial^2 w}{\partial x^2} \\ -\dfrac{\partial^2 w}{\partial y^2} \\ -2-\dfrac{\partial^2 w}{\partial x \partial y} \end{Bmatrix} \tag{6}$$

On the other hand, the total tensile energy equation of a rectangular plate at loads thought to be applied only to N_x's:

$$U = \iint_R \left(M_x\left(\frac{\partial^2 w}{\partial x^2}\right) + 2M_{xy}\left(\frac{\partial^2 w}{\partial x \partial y}\right) + M_y\left(\frac{\partial^2 w}{\partial y^2}\right)\right)dxdy + \iint_R \left(N_x \frac{\partial^2 w}{\partial x^2}\right)dxdy \tag{7}$$

Taking the first variation of the energy equation above, writing equal to zero and in matrix form:

$$U = \iint_R \left(\begin{bmatrix} M_x & M_y & M_{xy} \end{bmatrix} \delta \begin{Bmatrix} -\dfrac{\partial^2 w}{\partial x^2} \\ -\dfrac{\partial^2 w}{\partial y^2} \\ -2-\dfrac{\partial^2 w}{\partial x \partial y} \end{Bmatrix} \right) dxdy + \iint_R N_x \frac{\partial w}{\partial x} \delta \left(\frac{\partial w}{\partial x} \right) dxdy = 0 \tag{8}$$

by using Equations (5) and (6) and (8) this statement can be written as:

$$U = \iint_R \{\delta\varepsilon\}^T \frac{\mathrm{E}_1 e^{-\lambda x} h^3}{12(1-\nu^2)} \begin{bmatrix} 1 & \nu & 0 \\ \nu & 1 & 0 \\ 0 & 0 & \dfrac{1-\nu}{2} \end{bmatrix} \{\varepsilon\} dxdy + \iint_R N_x \frac{\partial w}{\partial x} \delta \left(\frac{\partial w}{\partial x} \right) dxdy = 0 \tag{9}$$

Hereinafter, the standard Finite Element procedure using Hermitian polynomials will be used. The following definitions are used to represent the Eq. (9) in nodal displacements, including the shape functions $\tilde{N}$'s generated from the Hermitian polynomials:

$$\{w\} = \left[\tilde{N}\right]\{a\} = \{a\}^T \left[\tilde{N}\right]^T \tag{10}$$

and

$$\delta w = \{\delta a\}^T \left[\tilde{N}\right]^T \tag{11}$$

where T means the transpose of a matrix and $\{a\}$ is the nodal displacement vector.
So, the node displacement vector for an element would be:

$$\{a\}^e = \begin{Bmatrix} a_i \\ a_j \\ a_k \\ a_l \end{Bmatrix} = \begin{Bmatrix} w \\ \theta_x \\ \theta_y \\ \theta_{xy} \\ . \\ . \\ . \end{Bmatrix} \tag{12}$$

Crucial ε as in the form $\{\varepsilon\} = [L]\{w\}$ and $[B] = [L]\left[\tilde{N}\right]$. Hence $\{\varepsilon\} = [B]\{a\}$

Substituting the above equation in Eq. (12) gives

$$\{\delta a\}^T \left(\iint_R [B]^T D_{FGM} \begin{bmatrix} 1 & \nu & 0 \\ \nu & 1 & 0 \\ 0 & 0 & \dfrac{1-\nu}{2} \end{bmatrix} [B] dxdy \right) \{a\} - \{\delta a\}^T \left[\iint_R \left(\left[\tilde{N}_{,x}\right]^T \left[\tilde{N}\right] dxdy \right) \{a\} \right] = 0 \tag{13}$$

Thus, the finite element equation will be in the compact form

$$\left[K_F\right]_{fgm}\{a\} - N_x\left[K_{Gx}\right]\{a\} \tag{14}$$

embodying an eigenvalue problem. $[K_F]$ and $[K_{Gx}]$ are Bending and geometric hardness matrices of FGM plate. Here, the modulus of elasticity of the plate and hence the stiffness matrix [D] must be calculated at the nodes due to its dependence on the x values. Thus, when finite elements are mounted on spherical matrices, the effect of the diversity of the modulus of flexibility is achieved by inserting it into it. But, changing the value λ to zero would be a homogeneous plate where the plate is clearly equal to E_0 along the elastic modulus.
For each element $[K_F]$ and $[K_{Gx}]$ as transmuted into a unit reference element there is

$$\left[K_F\right]^e = \int_{\eta=0}^{1}\int_{\xi=0}^{1}\left[B\right]^T D_{FGM}\begin{bmatrix} 1 & \nu & 0 \\ \nu & 1 & 0 \\ 0 & 0 & \dfrac{1-\nu}{2} \end{bmatrix}\left[B\right]\det\left(J\right)d\xi d\eta\,. \tag{15}$$

[B] matrix is described in shape functions and transformation matrices as:

$$\left[B\right] = \begin{Bmatrix} \left\langle \dfrac{\partial^2 N_0}{\partial x^2} \right\rangle \\ \left\langle \dfrac{\partial^2 N_0}{\partial y^2} \right\rangle \\ \left\langle \dfrac{\partial^2 N_0}{\partial x \partial y} \right\rangle \end{Bmatrix} = \left[T_1\right]\begin{Bmatrix} \left\langle \dfrac{\partial N_0}{\partial \xi} \right\rangle \\ \left\langle \dfrac{\partial N_0}{\partial \eta} \right\rangle \end{Bmatrix} + \left[T_2\right]\begin{Bmatrix} \left\langle \dfrac{\partial^2 N_0}{\partial \xi^2} \right\rangle \\ \left\langle \dfrac{\partial^2 N_0}{\partial \eta^2} \right\rangle \\ \left\langle \dfrac{\partial^2 N_0}{\partial \xi \partial \eta} \right\rangle \end{Bmatrix} \tag{16}$$

where

$$\left[T_2\right] = \begin{bmatrix} j_{11}^2 & j_{12}^2 & 2j_{11}j_{12} \\ j_{21}^2 & j_{22}^2 & 2j_{21}j_{22} \\ j_{11}j_{21} & j_{12}j_{22} & j_{11}j_{22} + j_{12}j_{21} \end{bmatrix} \tag{17}$$

and

$$\left[T_1\right] = -\left[T_2\right]\begin{bmatrix} \dfrac{\partial}{\partial \xi}J_{11} & \dfrac{\partial}{\partial \xi}J_{12} \\ \dfrac{1}{2}\left(\dfrac{\partial}{\partial \eta}J_{11} + \dfrac{\partial}{\partial \xi}J_{21}\right) & \dfrac{1}{2}\left(\dfrac{\partial}{\partial \eta}J_{12} + \dfrac{\partial}{\partial \xi}J_{22}\right) \end{bmatrix}\left[j\right] \tag{18}$$

In the above equations the J_{ij} and j_{ij} are the elements Jacobian and inverse Jacobian matrices of the transformation respectively. For two dimensional transformation the elements of Jacobian matrix are $J_{11} = \partial x / \partial \xi$, $J_{12} = \partial y / \partial \xi$, $J_{21} = \partial x / \partial \eta$, $J_{22} = \partial y / \partial \eta$.
As the flexural stiffness matrix $[K_F]$ carries the effect of the elasticity modulus change the geometric rigidity matrix $[K_{Gx}]$ carries the effect of the plate's and considering the equilibrium of the forces will be in the form:

$$[K_{Gx}]^e = \int_{\eta=0}^{1}\int_{\xi=0}^{1} \frac{b_1}{b_1 + 2x\tan\theta}\left(j_{11}N_\xi + j_{12}N_\eta\right)\left\langle j_{11}N_\xi + j_{12}N_\eta\right\rangle d\xi d\eta \tag{19}$$

The coordinate x in the real plane is also transformed into the reference plane in both $[K_F]$ and $[K_{Gx}]$ matrices by $x = (\xi-1)(\eta-1)x_1 - \xi(\eta-1)x_2 + \xi\eta x_3 - \eta(\xi-1)x_4$ attained from the transformation polynomials. Here x_1,.., x_4 are the x coordinates of a real element. In Equation (19) simple taking the θ value as zero reach the geometric matrix of a rectangular plate.
Varying elasticity modulus along z-axis to obtain the effect of the change of elasticity modulus along the thickness the same procedure is applied but this time the [D] matrix of the FGM plate includes the integral of the elasticity modulus along the z-axis. Thus, Eq. (2) will be in the form if an E(z) function as in the Equation $E = (E_t - E_b)\left(\frac{2z+h}{2h}\right)^n + E_b$:

$$[D]_{fgm} = \frac{1}{(1-\nu^2)}\begin{bmatrix} 1 & \nu & 0 \\ \nu & 1 & 0 \\ 0 & 0 & \frac{1-\nu}{2} \end{bmatrix} \int_{-h/2}^{h/2} \left\{(E_1 - E_2)(\frac{2z+h}{2h})^n + E_2\right\} z^2 dz \tag{20}$$

Although the integral along the z-axis can be calculated analytically as

$$\int_{-h/2}^{h/2} \left\{(E_1 - E_2)(\frac{2z+h}{2h})^n + E_2\right\} z^2 dz \tag{21}$$

$$= \frac{(E_1 - E_2)h^3}{1-\nu^2}\frac{n^2+n+2}{4(n+1)(n+2)(n+3)} + \frac{E_2 h^3}{12(1-\nu^2)}$$

it is convenient to calculate its value by any of the numerical integral methods such as Gaussian Quadrature method to provide its applicability to a numerical computation [24]. This time in the Equation (20) E_1 and E_2 denotes the upper and lower surfaces' elasticity modulus of the plate respectively. The effect of the elasticity modulus change in the z-direction is inserted by the $[D]_{fgm}$ matrix. Obviously, choosing n=0 the results pertaining to a homogenous case can be reached for the plate which has the elasticity modulus E_1.
Thus the flexural stiffness matrix will be as

$$[K_F]^e = \int_{\eta=0}^{1}\int_{\xi=0}^{1} [B]^T [D]_{fgm} [B] \det(J) d\xi d\eta \tag{22}$$

For the geometric stiffness matrix $[K_{Gx}]$ of the trapezoidal plate Equation (19) is still valid.

5. Results and Discussions

Figures (2,7) show comparison of FEM and ANSYS evolution of critical buckling loads N_x of FGM plate power law index n with aspect ratio a/b=0.25;0.5;0.75;1.0 at CFFC and FFFC boundary conditions for the elasticity modulus varies according to the function $E(x) = (E_1 - E_2)(\frac{x+L}{2L})^n + E_2$ and $E(x)=E_1e^{-\lambda x}$. Results pertaining to a rectangular FGM plate have been investigated first for various variation of elasticity modulus both along the thickness and along the x-axis. Ceramic-metal material composition of FGM plate has been selected due to fact that this configuration finds plentiful application in the industry. When ceramic side is selected to be alumina the elasticity modulus E=380x10^9 GPa and Poisson's ratio υ=0.3 In addition to this the metal side has properties E=70x10^9 GPa and υ=0.3 when the metal is aluminum. Various ceramic-metal configurations can be selected for various applications. In order to find the effect of these indices on the stability of the FGM plate, buckling of loads against power indices λ and n is given. According to the material and geometric properties used in numerical method model, commercial (ANSYS) finite element code is produced by comparing [25]. Shell models are applied to illustrate how plane mesh size affects the accuracy of buckling analysis for plates of various length ratios and thicknesses in ANSYS. In the finite element model, the Shell281 element is used with various values of plane mesh size, expressed as element per plate edge, and in various thickness values, expressed as the half-thickness ratio up to thin to medium FGM plates. The Shell281 model uses the observation size of 80 and 100 elements per side for each side thickness ratio. The variations of critical buckling loads in FGM*)* plate for different boundary conditions are shows in Fig.2-7. The effect of power law index n and λ on the critical buckling loads can be seen for different boundary conditions. Figs.2-7 shows the critical buckling loads verses power law index value at different boundary conditions. As expected, the increasing index value leads to reduce the critical buckling loads. Increasing index value reduces the ceramic constituents, it produces the effective material properties changes which affect the critical buckling loads.

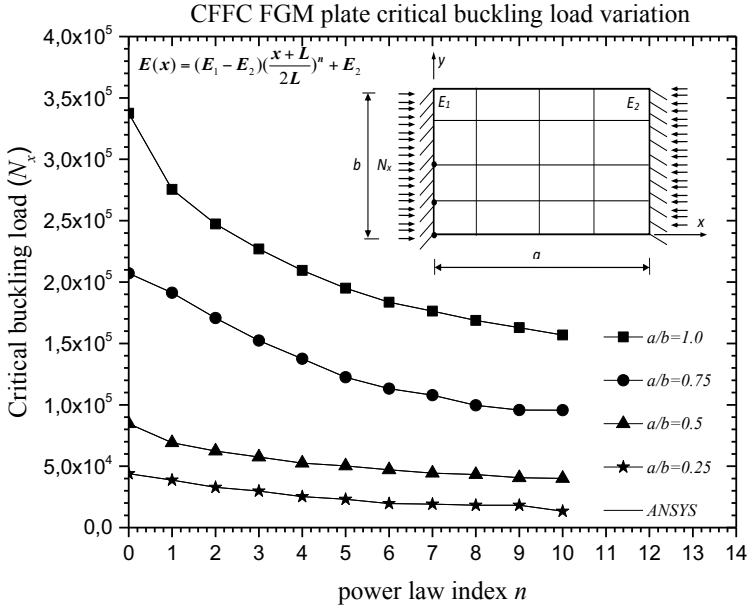

Fig. 2. Critical buckling load of FGM plate verses power law index n with aspect ratio a/b=0.25;0.5;0.75;1.0 at CFFC boundary conditions for the elasticity modulus varies according to the function $E(x) = (E_1 - E_2)(\frac{x+L}{2L})^n + E_2$

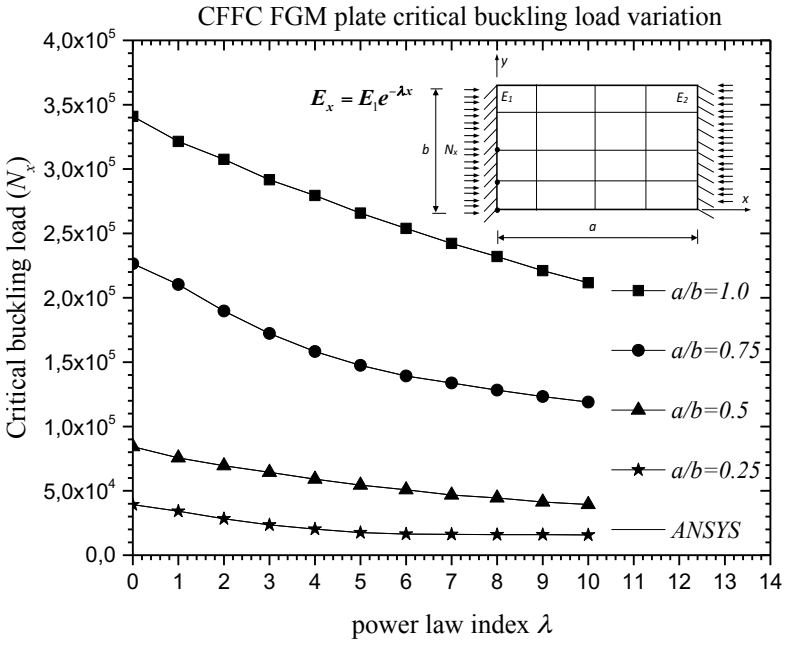

Fig. 3. Critical buckling load of FGM plate verses power law index λ with aspect ratio a/b=0.25;0.5;0.75;1.0 at CFFC boundary conditions for the elasticity modulus varies according to the function $E(x)=E_1e^{-\lambda x}$

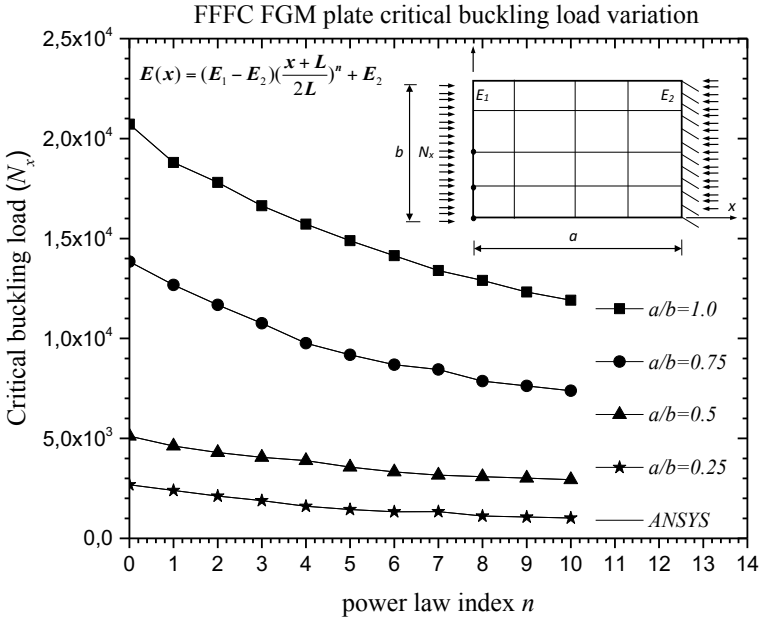

Fig. 4. Critical buckling load of FGM plate verses power law index n with aspect ratio a/b=0.25;0.5;0.75;1.0 at FFFC boundary conditions for the elasticity modulus varies according to the function $E(x) = (E_1 - E_2)(\frac{x+L}{2L})^n + E_2$

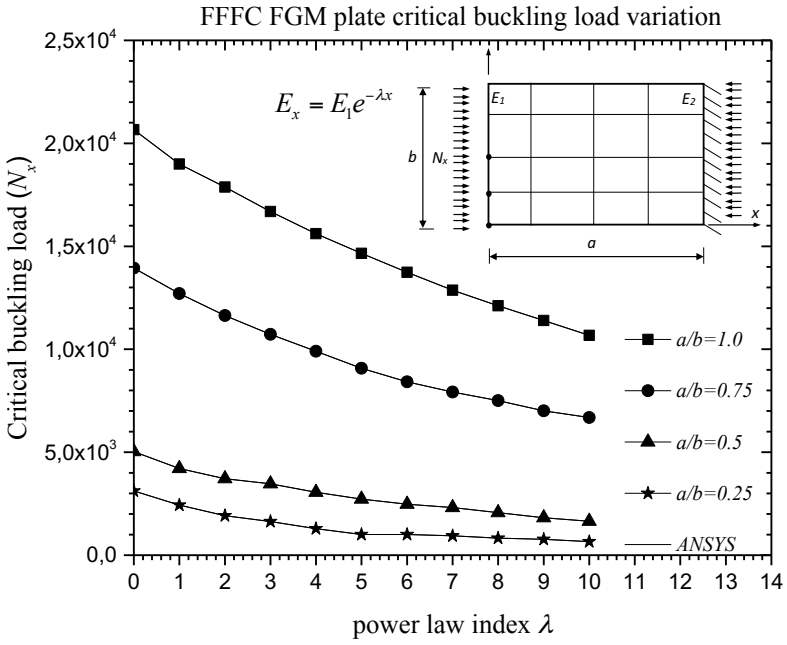

Fig. 5. Critical buckling load of FGM plate verses power law index λ with aspect ratio a/b=0.25;0.5;0.75;1.0 at FFFC boundary conditions for the elasticity modulus varies according to the function $E(x)=E_1 e^{-\lambda x}$

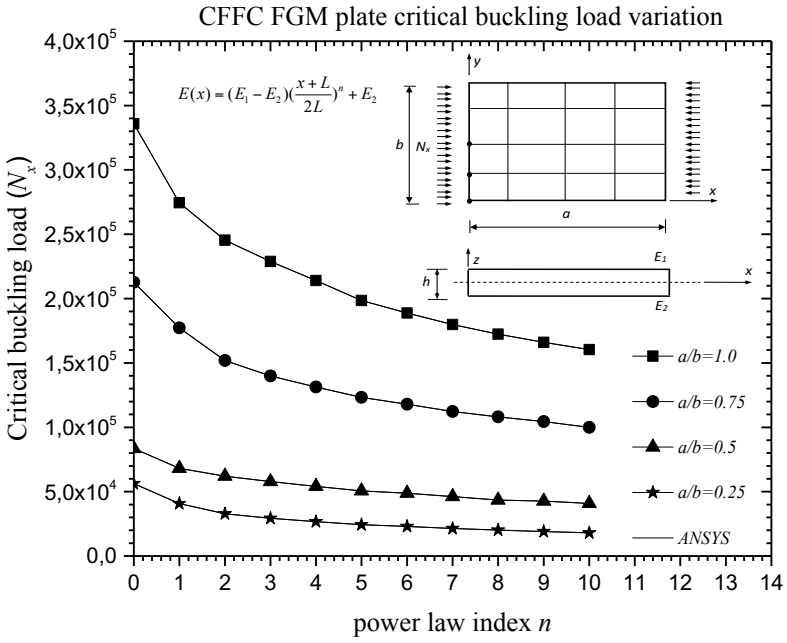

Fig. 6. Critical buckling load of FGM plate verses power law index n with aspect ratio a/b=0.25;0.5;0.75;1.0 at CFFC boundary conditions for the elasticity modulus varies according to the function $E(x) = (E_1 - E_2)(\frac{x+L}{2L})^n + E_2$

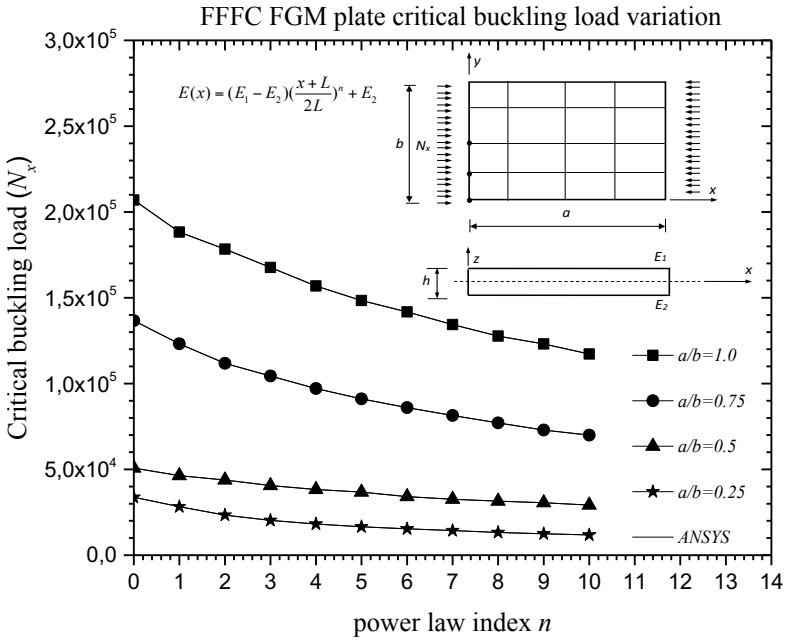

Fig. 7. Critical buckling load of FGM plate verses power law index n with aspect ratio a/b=0.25;0.5;0.75;1.0 at FFFC boundary conditions for the elasticity modulus varies according to the function $E(x) = (E_1 - E_2)(\frac{x+L}{2L})^n + E_2$

6. Conclusion

The stability behavior of rectangular FGM plates under various boundary conditions is investigated using the finite element method. The ceramic-metal (Alumina-Aluminum) composition of FGM has been chosen to obtain numerical results. Two types of boundary conditions have been studied CFFC configuration and FFFC configuration. In order to justify the proposed model, a homogeneous rectangular plate condition is considered. The results obtained for the CFFC configuration were observed to have lower critical buckling loads than those obtained for the FFFC configuration. The latter is less stable. This applies to both homogeneous and FGM plates. Increasing the power law indices (λ and n) makes the plate less stable. At large values of these indices, the plate achieves an unstable behavior as if there were no restrictions along the plates and thus buckles easily. This negative impact of the power index should be considered during the design of the structures. The effect of the metal-ceramic composition (the properties of the components of the FGM plate), the power law indices determining the amount of the composition, the dimensions of the plate, the angle of inclination and the boundary conditions affect the stability of the plate. Good configuration of these parameters will ensure that the structure has the optimum critical buckling load value. Although the specified parameters have limitations with respect to each other, optimum configurations can be obtained according to use by observing their effects separately.

References

[1] Levy, S., *Bending of rectangular plates with large deflections*. 1942: US Government Printing Office.

[2] Javaheri, R. and M. Eslami, Buckling of Functionally Graded Plates under In- plane Compressive Loading. *ZAMM- Journal of Applied Mathematics and Mechanics/Zeitschrift für Angewandte Mathematik und Mechanik: Applied Mathematics and Mechanics,* 82, 277-283, 2002

[3] Chen, X. and K. Liew, Buckling of rectangular functionally graded material plates subjected to nonlinearly distributed in-plane edge loads. *Smart Materials and Structures,* 13, 1430, 2004

[4] Vel, S.S. and R. Batra, Three-dimensional exact solution for the vibration of functionally graded rectangular plates. *Journal of Sound and Vibration,* 272, 703-730, 2004

[5] Chi, S.-H. and Y.-L. Chung, Mechanical behavior of functionally graded material plates under transverse load—Part I: Analysis. *International Journal of Solids and Structures,* 43, 3657-3674, 2006

[6] Shariat, B.S. and M. Eslami, Buckling of thick functionally graded plates under mechanical and thermal loads. *Composite Structures,* 78, 433-439, 2007

[7] Birman, V. and L.W. Byrd, Modeling and analysis of functionally graded materials and structures. 2007

[8] Shahrjerdi, A., F. Mustapha, M. Bayat, S. Sapuan, R. Zahari, and M. Shahzamanian. *Natural frequency of FG rectangular plate by shear deformation theory*. in *IOP conference series: materials science and engineering*. 2011. IOP Publishing.

[9] Zhang, D.-G. and Y.-H. Zhou, A theoretical analysis of FGM thin plates based on physical neutral surface. *Computational Materials Science,* 44, 716-720, 2008

[10] Prakash, T., M. Singha, and M. Ganapathi, Influence of neutral surface position on the nonlinear stability behavior of functionally graded plates. *Computational mechanics,* 43, 341-350, 2009

[11] Mohammadi, M., A. Saidi, and E. Jomehzadeh, A novel analytical approach for the buckling analysis of moderately thick functionally graded rectangular plates with two simply-supported opposite edges. *Proceedings of the Institution of Mechanical Engineers, Part C: Journal of Mechanical Engineering Science,* 224, 1831-1841, 2010

[12] Talha, M. and B. Singh, Static response and free vibration analysis of FGM plates using higher order shear deformation theory. *Applied Mathematical Modelling,* 34, 3991-4011, 2010

[13] Pendhari, S.S., T. Kant, Y.M. Desai, and C.V. Subbaiah, Static solutions for functionally graded simply supported plates. *International Journal of Mechanics and Materials in Design,* 8, 51-69, 2012

[14] Singha, M., T. Prakash, and M. Ganapathi, Finite element analysis of functionally graded plates under transverse load. *Finite elements in Analysis and Design,* 47, 453-460, 2011

[15] Hosseini-Hashemi, S., M. Fadaee, and S.R. Atashipour, Study on the free vibration of thick functionally graded rectangular plates according to a new exact closed-form procedure. *Composite Structures,* 93, 722-735, 2011

[16] Bousahla, A.A., S. Benyoucef, A. Tounsi, and S. Mahmoud, On thermal stability of plates with functionally graded coefficient of thermal expansion. *Structural Engineering and Mechanics,* 60, 313-335, 2016

[17] Demirhan, P.A. and V. Taskin, Levy solution for bending analysis of functionally graded sandwich plates based on four variable plate theory. *Composite Structures,* 177, 80-95, 2017

[18] Mohseni, E., A. Saidi, and M. Mohammadi, Bending-stretching analysis of thick functionally graded micro-plates using higher-order shear and normal deformable plate theory. *Mechanics of Advanced Materials and Structures,* 24, 1221-1230, 2017

[19] Akgöz, B. and Ö. Civalek, A size-dependent beam model for stability of axially loaded carbon nanotubes surrounded by Pasternak elastic foundation. *Composite Structures,* 176, 1028-1038, 2017

[20] Civalek, Ö. and O. Kiracioglu, Free vibration analysis of Timoshenko beams by DSC method. *International Journal for Numerical Methods in Biomedical Engineering,* 26, 1890-1898, 2010

[21] Civalek, O. and A. Yavas, Large deflection static analysis of rectangular plates on two parameter elastic foundations. *International journal of science and technology,* 1, 43-50, 2006

[22] Mercan, K., Ç. Demir, and Ö. Civalek, Vibration analysis of FG cylindrical shells with power-law index using discrete singular convolution technique. *Curved and Layered Structures,* 1, 2016

[23] Timoshenko, S. and J. Goodier, *Theory of elasticity 3rd edition*. 1970, New York, McGraw-Hill.

[24] Woo, J. and S. Meguid, Nonlinear analysis of functionally graded plates and shallow shells. *International Journal of Solids and structures,* 38, 7409-7421, 2001

[25] ANSYS, A., V11 Program Documentation. *Ansys Inc., Canonsburg, Pennsylvania*,